Multipole expansion of the local expansion rate

Basheer Kalbouneh,[*] Christian Marinoni,[†] and Julien Bel[‡]
Aix Marseille Univ, Université de Toulon, CNRS, CPT, Marseille, France

(Received 1 November 2022; accepted 29 November 2022; published 4 January 2023)

We design a new observable, the expansion rate fluctuation η, to characterize deviations from the linear relation between redshift and distance in the local universe. We also show how to compress the resulting signal into spherical harmonic coefficients in order to better decipher the structure and symmetries of the anisotropies in the local expansion rate. We apply this analysis scheme to several public catalogs of redshift-independent distances, the Cosmicflows-3 and Pantheon datasets, covering the redshift range $0.01 < z < 0.05$. The leading anisotropic signal is stored in the dipole. Within the standard cosmological model, it is interpreted as a bulk motion (307 ± 23 km/s) of the entire local volume in a direction aligned at better than 4 degrees with the bulk component of the Local Group (LG) velocity with respect to the cosmic microwave background (CMB). This term alone, however, provides an overly simplistic and inaccurate description of the angular anisotropies of the expansion rate. We find that the quadrupole contribution is non-negligible (∼50% of the anisotropic signal), in fact, statistically significant, and signaling a substantial shearing of gravity in the volume covered by the data. In addition, the 3D structure of the quadrupole is axisymmetric, with the expansion axis aligned along the axis of the dipole. Implications for the determination of the H_0 parameter are discussed. We find that Hubble constant estimates may show variation as high as $\Delta H_0 = (4.1 \pm 1.1)$ km/s/Mpc between antipodal directions along the dipole axis. In the case of the Pantheon sample, this systematic difference is reduced to $\Delta H_0 = (2.4 \pm 1.1)$ km/s/Mpc once model-dependent correction for peculiar velocity flows are implemented. Notwithstanding, the axial anisotropy in the general direction of the CMB dipole is still detected. We thus show how to optimally subtract redshift anisotropies from Pantheon data in a fully model-independent way by exploiting the η observable. As a result, the value of the best fitting H_0 is systematically revised upwards by nearly 0.7 km/s/Mpc (about 2σ) compared to the value deduced from the Hubble diagram using the uncorrected observed redshift. The goodness of fit is also improved.

DOI: 10.1103/PhysRevD.107.023507

I. INTRODUCTION

In accordance with the cosmological principle (*CP*), the spatial sections of the universe are maximally symmetric, that is, rotationally and translationally invariant (e.g., [1]). This statement about the symmetries of the universe, sealed in the Robertson and Walker line element, can only be interpreted in a statistical sense, after convolving the spatial distribution of matter with large smoothing kernels. This makes its empirical confirmation difficult and subject to nontrivial systematicity.

Despite observational hurdles (e.g., [2]), convincing proofs of isotropy are provided by the angular distribution of the temperature fluctuations of the cosmic microwave background (CMB) [3,4]. Also, 3D supporting evidence continues to grow as spectroscopic studies reveal the structure of ever larger and deeper regions of the universe [5–14]. Analysis of the spatial distribution of supernovae, i.e., objects whose distances are estimated using redshift independent techniques, also provides tentative confirmation [15–22]. The nature of the confirmations remains preliminary, however, and there is no shortage of evidence to the contrary [23–37]. If some of these signals are not statistically significant enough to reject outright the *CP*, others appear as improbable in the framework of the standard cosmological model.

However, it has long been known that in the local outskirts of the Milky Way, at scales $r < 150h^{-1}$ Mpc, the *CP* is violated (e.g., [38,39]). This region represents about half of the volume used to determine the Hubble parameter H_0, a fundamental constant of the standard model and a consequence of the cosmological principle hypothesis. Traditionally, deviations from *CP* predictions are treated perturbatively by expanding the cosmological quantities into a smooth background component and a fluctuating part. Among the latter, a central role is occupied by peculiar velocities. These super-Hubble motions contain a lot of interesting cosmological information (e.g., [40])

[*]basheer.kalbouneh@cpt.univ-mrs.fr
[†]christian.marinoni@cpt.univ-mrs.fr
[‡]julien.bel@cpt.univ-mrs.fr

and indeed their amplitude confirms that the deviations from the *CP* are in general agreement with the limits imposed by the perturbation theory of the standard cosmological model (e.g. [41–44]). However, it was soon realized that many subtle systematic errors, if not properly subtracted, can compromise their use as efficient cosmological probes; non-Gaussian issues, homogeneous and inhomogeneous Malmquist biases, and incompleteness of mass catalogs used to predict the amplitude of peculiar velocities are among the pitfalls that most hamper the analysis [45].

In order to free the investigation of local inhomogeneities from certain statistical and observational complications, we explore in this paper another direction. We develop a completely nonperturbative approach to inhomogeneities that focuses directly on the scale factor of the universe as a relevant variable to quantify deviations from uniformity (see also [46,47] for a similar approach). This is precisely the parameter that is kept invariant in perturbative analyses, defining the reference background against which deformations in the spatial sector of the metric are compared.

In this spirit, we design an observable, the expansion rate fluctuation η, that provides information about fluctuations in the local expansion rate and is, at the same time, easily comparable with theoretical predictions. Indeed we will show that it provides a model-independent means of analyzing inhomogeneities, not even requiring the *CP* assumption as a prerequisite. This cosmographic approach (e.g. [48,49]) allows the results to be directly interpretable in alternative spacetimes and can ideally guide the search for unconventional line elements that capture the essential features of the local inhomogeneities.

From an observational point of view, the goal is to investigate the existence and significance of anisotropies in the local universe through new methods of investigation; in this specific case, by decomposing the angular fluctuations of the expansion rate into spherical harmonics and compressing information about anisotropies into a set of independent Fourier coefficients.

Multipolar expansion in spherical harmonics provides an orthogonal insight into the nature of the local redshift-distance relation and allows to go beyond the simple dipole model with which anisotropies are traditionally described in the nearby universe. At the same time, it allows to deepen and extend studies, such as those of [38,47,50–52] which attempt to constrain the tidal field component by analyzing the shear of the velocity field generated by local gravitational fluctuations. In this respect, we focus on the study of the symmetries and geometric structure of the harmonic multipoles, showing how their analysis gives a simple and inexpensive description of the structure of the anisotropies in the Hubble flow. We demonstrate that the three-parameter formula encoding such information has predictive power comparable to that of much more complex numerical studies of peculiar motions.

The paper is organized as follows: in Sec. II we introduce the observable that optimally extract information about the fluctuation in the angular expansion rate, while in III we present the method implemented to estimate the signal from discrete datasets and to compress it into spherical harmonic coefficients. We also discuss how we estimate reconstruction errors, both statistical and systematic. In Sec. IV, we describe the data analyzed. Results are presented and interpreted in V. Section VI provides the summary and conclusion. In the following, we present results in natural units ($c = 1$) and we refer to the standard ΛCDM model, as the flat Friedmann-Robertson-Walker (FRW) spacetime which best fits the Planck18 data [53]. Redshift is expressed with respect to the CMB rest frame.

II. THE EXPANSION RATE FLUCTUATIONS η

We model the angular anisotropies in the redshift-distance relation by directly exploiting the local expansion rate as a target observable. In a perfectly uniform FRW universe, the ratio z/d between the redshift and the proper distance of comoving particles is predicted to be constant, independent from the particular line-of-sight along which it is estimated.

In any generic metric model describing the structure of local spacetime, i.e. the inhomogeneous distribution of mass at the periphery of the Local Group of galaxies, it is possible, at least in the limit of small separations, to relate the observed redshift z and the proper distance as follows:

$$z = \tilde{H}_0(l, b)d. \tag{1}$$

In this expression, $\tilde{H}_0$ is a continuous function that depends only on the angular coordinates (l, b) and can be constrained experimentally. It is clear that the angular dependence is in principle theoretically determinable as soon as a line element is provided. Note that if the observer is only at rest relative to the CMB, but not comoving with respect to the surrounding matter, then we expect a dependence of $\tilde{H}_0$ on the radial distance even in very local regions of the Universe. As a matter of fact, in a generic spacetime, the characteristic distance scale at which the linear limit of the Eq. (1) is reached is not known apriori.

We actually characterize deviations from isotropy in the local expansion rate via the (decimal) logarithmic relation

$$\eta \equiv \log\left[\frac{\tilde{H}_0}{H_0}\right]. \tag{2}$$

Here H_0 is a normalizing factor that, in the standard model of cosmology, coincides with the value of the Hubble constant. We fix its amplitude by requiring that the average value of η over the volume covered by data vanishes.

The justification for the choice of this observable is statistical in nature. Errors are Gaussian only in the distance modulus μ and not in the redshift-independent distance d if these latter are estimated as

$$\hat{d} = 10^{\frac{\mu-25}{5}}. \tag{3}$$

Therefore, given a sample of objects at spatial position $\mathbf{r}$, the discrete estimator of the continuous field (2),

$$\hat{\eta}(\mathbf{r}) = \log\left[\frac{z}{H_0}\right] + 5 - \frac{\mu}{5}, \tag{4}$$

is a random variable that follows a Gaussian distribution. Indeed, we assume that the uncertainty δ on $\hat{\eta}$ is induced only by the imprecision with which the redshift-independent distances are estimated ($\delta = \sigma_\mu/5$), i.e. we consider that any error in the redshift estimate is negligible. As a consequence, $\hat{\eta}$ provides an unbiased estimate of η, as can be easily verified. As an added bonus, Eq. (2) also makes it possible to quantify anisotropies in the expansion rate, regardless of the value of the Hubble constant parameter used to normalize the distance modules μ. A subtlety must be pointed out. It is implicitly assumed, in the above argument, that in the limit $z \ll 1$, the range we are concerned with in this paper, d is a fair proxy for both the luminosity and angular diameter distance, i.e. $d \approx d_L \approx d_A$.

The expansion rate fluctuation η is not specifically tailored to have only nice statistical properties. It also has a physical content. Linear perturbation theory of the standard cosmological model provides a framework for interpreting this observable. According to it, the redshift observed in the CMB rest frame is given by

$$z = z_c + v(1 + z_c), \tag{5}$$

where z_c is the cosmological redshift and v is the line-of-sight component of the peculiar velocity of the source (assumed to be nonrelativistic) with respect to the CMB rest frame. By inserting this last relation into (2) we get

$$\eta = \log\left(1 + \frac{v(1+z_c)}{z_c}\right) \approx \frac{v(1+z)}{z \ln 10}, \tag{6}$$

where we have assumed $v \ll z_c \approx z$. The fluctuations in the expansion rate are excited by radial peculiar velocity and suppressed in inverse proportion to the object's distance.

III. EXPANSION RATE FLUCTUATIONS: THE SPHERICAL HARMONIC DECOMPOSITION

We can compress the information contained in the η observable into a few coefficients. To this end, we expand the expansion rate field η in spherical harmonic (SH) components. We orthogonally decompose η on a sphere as follows:

$$\eta = \sum_{\ell=0}^{\infty} \sum_{m=-\ell}^{\ell} a_{\ell m} Y_{\ell m}(\theta, \phi) = \sum_{\ell=0}^{\infty} \eta_\ell, \tag{7}$$

where

$$Y_{\ell m}(\theta, \phi) = \sqrt{\frac{(2\ell+1)(\ell-m)!}{4\pi(\ell+m)!}} P_\ell^m(\cos\theta) e^{im\phi}, \tag{8}$$

and P_ℓ^m are associated Legendre polynomials. Thus, the Fourier coefficients $a_{\ell m}$ can be expressed as

$$a_{\ell m} \equiv \int_0^{2\pi} \int_0^{\pi} \eta(\theta, \phi) Y^*_{\ell m}(\theta, \phi) \sin\theta \, d\theta d\phi. \tag{9}$$

Note that, due to the definition, the monopole ($\ell = 0$) of η vanishes.

In addition, one can define the angular power spectrum of the η anisotropy as

$$C_\ell = \langle |a_{\ell m}|^2 \rangle_e, \tag{10}$$

where the expectation is intended to be over a statistical ensemble of universes:

$$\hat{C}_\ell = \frac{1}{2\ell+1} \sum_{m=-\ell}^{\ell} |a_{\ell m}|^2 \tag{11}$$

is an unbiased estimator for C_ℓ

Section III A describes in detail the procedure adopted to reconstruct the field $\eta(\Omega)$ from discrete 3D data with nonuniform sampling rates on the sky. In Sec. III B we describe how the SH coefficients $a_{\ell m}$ are estimated. We present the analytical formulas and numerical recipes for evaluating measurement errors, both statistical and systematic, in the Secs. III C and III D, respectively.

A. Estimation of the angular η field

The expansion rate fluctuation estimator $\hat{\eta}(\mathbf{r})$ is a discrete random variable. The analysis of this observable can be simplified, and the underlying theoretical model (2) can be better traced if we convert it into a stochastic field. We thus average $\hat{\eta}(\mathbf{r})$ over all the objects at position $\mathbf{r}$ within a given volume $V(\Omega, R)$, where Ω is a solid angle centered on the observer and R is the depth of the catalog (i.e. its upper edge). The angular anisotropies seen by the observer are thus piecewise defined as

$$\eta(\Omega) = \frac{\sum_i^N \hat{\eta}(\mathbf{r}_i) w(\mathbf{r}_i) W(\mathbf{r}_i | V(\Omega, R))}{\sum_i^N w(\mathbf{r}_i) W(\mathbf{r}_i | V(\Omega, R))}, \tag{12}$$

where N is the number of objects in the catalog, $w(\mathbf{r}_i) = 1/\delta_i^2$ is a weight that takes into account the precision in the measurement of the distance of the ith object in the catalog. $W(\mathbf{r}|V(\Omega, R))$ is a window function which evaluates to unity if $\mathbf{r}_i \in V$ and is null otherwise.

It is clear that averaging has the advantage of reducing noise at the cost of a lower angular resolution. The latter is essentially controlled by the aperture of the solid angle Ω, although it also depends, in principle, on the depth R of the sample on which the spatial averaging is performed.

In practice, we construct the η 2D field out of a discrete point process $\hat{\eta}(\mathbf{r})$, by first partitioning the sky in N_{pix}

identical pixels (each subtending a solid angle Ω_i) using HEALPIX [54] and then by applying Eq. (12) to objects within the volume V subtended by each pixel Ω_i. HEALPIX is an algorithm which tessellates a spherical surface into curvilinear quadrilaterals, each covering the same area as every other. Although characterized by a different shape, the resulting pixels are located on lines of constant latitude. This property is essential for speeding up computation but is less than optimal for pixelating the discrete η field. In fact, the counts can show large variations from pixel to pixel. In addition, some of the pixels may end up containing no data at all. To tackle this issue, we first rigidly rotate the galaxy field randomly, by looking for configurations in which all the HEALPIX pixels are filled with objects *and* the least populated cell contains a maximum number of objects. If as a result of different rotations, the maximum number of galaxies in the least populated cells stays the same, we pick up the configuration for which the distribution of the number of the galaxies in the pixels has the minimum variance. This allows to minimize pixel-to-pixel fluctuations in the reconstructed value of η and increase the signal-to-noise ratio in the determination of the Fourier coefficients. Note that the rotation trick does not affect the estimation of the angular power spectrum $\hat{C}_\ell$, which is, by definition, invariant under rotation. However, once the Fourier coefficients have been estimated, we apply an inverse rotation to the pixels and η maps so that, for the sake of clarity, the results are presented in standard galactic (l, b) coordinates. The whole strategy is graphically illustrated in Fig. 1.

The resolution of the HEALPIX grid is calculated as $N_{\rm pix} = 12N_{\rm side}^2$, where $N_{\rm side} = 2^t$, and $t \in \mathbb{N}$. The baseline grid, corresponding to $t = 0$, has 12 pixels. Our choice of the resolution in the reconstruction of the angular η map, as explained in V, is dictated by two criteria: the SH decomposition must result in multipoles that have a sufficiently high signal-to-noise ratio and a sufficiently low probability p to occur by chance in a randomly fluctuating η field.

B. Estimation of the SH coefficients

We estimate the Fourier coefficients of the spherical harmonic decomposition by slightly modifying the reconstruction scheme provided by the HEALPIX algorithm. HEALPIX accomplishes that by means of an iteration scheme, the so-called *Jacobi iteration*. The zeroth order estimator of the coefficients of the expansion field is

$$\hat{a}^{(0)}_{\ell m} = \frac{4\pi}{N_{\rm pix}} \sum_{p=1}^{N_{\rm pix}} \eta(\Omega_p) Y^*_{\ell m}(\theta_p, \phi_p), \tag{13}$$

where (θ_p, ϕ_p) are the angular coordinates of the center of each pixel p and $\eta(\Omega_p)$ is calculated by Eq. (12). The Fourier coefficients $a_{\ell m}$ are then calculated up to the order $\ell_{\rm max} = 3N_{\rm side} - 1$, and the higher orders are

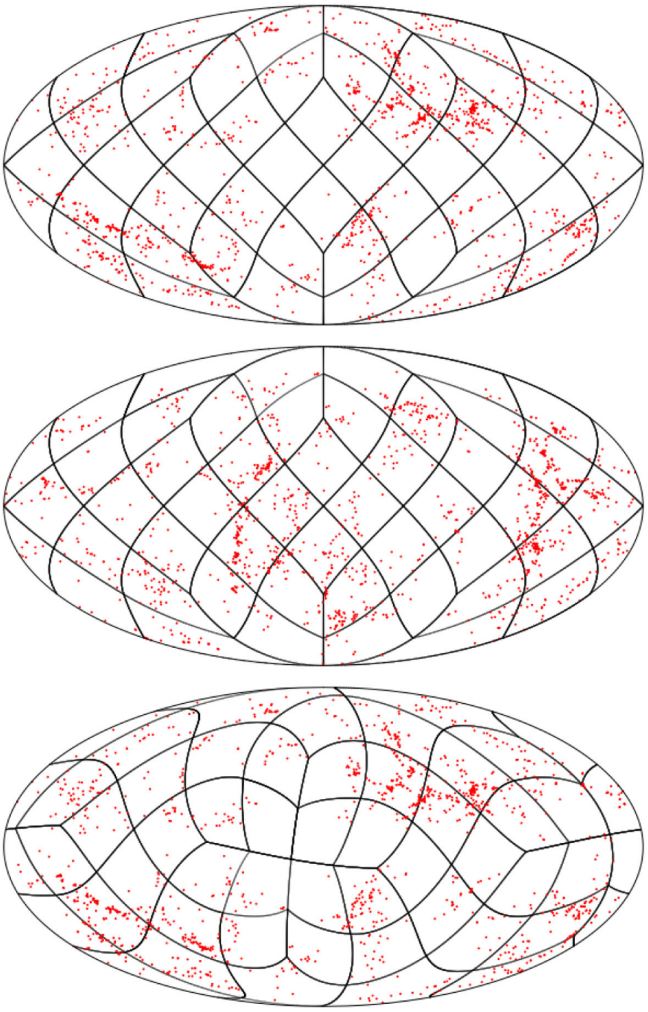

FIG. 1. Illustration of the rotation strategy to improve the estimation of SH coefficients. Upper: the standard HEALPIX pixels ($N_{\rm side} = 2$ and $N_{\rm pix} = 48$) tessellating the distribution of galaxies in the galactic coordinates. Note the presence of an empty pixel. Center: rigid rotation applied to the sample so that in each pixel falls at least one galaxy (the minimum number is 5 in this example). Lower: the inverse rotation is applied to both galaxies and pixels.

$$\hat{a}^{(k+1)}_{\ell m} = \hat{a}^{(k)}_{\ell m} + \frac{4\pi}{N_{\rm pix}} \sum_{p=1}^{N_{\rm pix}} (\eta(\Omega_p) - \eta^{(k)}(\theta_p, \phi_p)) Y^*_{\ell m}(\theta_p, \phi_p), \tag{14}$$

where

$$\eta^{(k)}(\theta_p, \phi_p) = \sum_{\ell=0}^{\ell_{\rm max}} \sum_{m=-\ell}^{\ell} \hat{a}^{(k)}_{\ell m} Y_{\ell m}(\theta_p, \phi_p). \tag{15}$$

In matrix notation,

$$\boldsymbol{a}^{(0)} = \boldsymbol{A}\boldsymbol{\eta} \tag{16}$$

$$\boldsymbol{a}^{(k+1)} = \boldsymbol{a}^{(k)} + \boldsymbol{A}(\boldsymbol{\eta} - \boldsymbol{\eta}^{(k)}) \tag{17}$$

$$\boldsymbol{\eta}^{(k)} = \boldsymbol{S}\boldsymbol{a}^{(k)}, \tag{18}$$

where $\boldsymbol{a}$ is the vector of the spherical harmonic coefficients [containing $(\ell_{\max}+1)^2$ elements], while $\boldsymbol{\eta}$ and $\boldsymbol{\eta}^{(k)}$ are vectors representing the measured and estimated values of η in each pixel (and thus contain $N_{\rm pix}$ elements). Moreover, $\boldsymbol{A} = \frac{4\pi}{N_{\rm pix}} Y^*_{\ell m}(\theta_p, \phi_p)$ and $\boldsymbol{S} = \frac{N_{\rm pix}}{4\pi}\boldsymbol{A}^{*T}$. The calculation of $\boldsymbol{a}^{(k)}$ is repeated until convergence, i.e. until the residual has zero Fourier coefficients up to $\ell_{\max}$.

Instead of going through the iteration scheme, we proceed in a different way. We estimate analytically the asymptotic limit $\boldsymbol{a}^{(\infty)}$ that should be ideally obtained in the limit of an infinite number of iterations. We first write Eq. (17) as

$$\boldsymbol{a}^{(k+1)} = \boldsymbol{a}^{(k)} + \boldsymbol{A}\boldsymbol{\eta} - \boldsymbol{A}\boldsymbol{S}\boldsymbol{a}^{(k)}, \tag{19}$$

so

$$\boldsymbol{a}^{(k+1)} = \boldsymbol{A}\boldsymbol{\eta} + (\boldsymbol{I} - \boldsymbol{A}\boldsymbol{S})\boldsymbol{a}^{(k)}, \tag{20}$$

where $\boldsymbol{I}$ is the identity matrix with size $(\ell_{\max}+1)^2 \times (\ell_{\max}+1)^2$. By using $\boldsymbol{a}^{(0)} = \boldsymbol{A}\boldsymbol{\eta}$ we obtain

$$\boldsymbol{a}^{(k+1)} = \boldsymbol{a}^{(0)} + (\boldsymbol{I} - \boldsymbol{A}\boldsymbol{S})\boldsymbol{a}^{(k)}. \tag{21}$$

Under the assumption that this is convergent, for $k \to \infty$, $\boldsymbol{a}^{(k+1)} \to \boldsymbol{a}^{(k)}$ we get

$$\boldsymbol{a}^{(\infty)} = \boldsymbol{a}^{(0)} + (\boldsymbol{I} - \boldsymbol{A}\boldsymbol{S})\boldsymbol{a}^{(\infty)}, \tag{22}$$

which results in

$$\boldsymbol{a}^{(\infty)} = \boldsymbol{M}\boldsymbol{a}^{(0)}, \tag{23}$$

where $\boldsymbol{M} = (\boldsymbol{A}\boldsymbol{S})^{-1}$. Note that we cannot take the inverse of $\boldsymbol{A}$ or $\boldsymbol{S}$ individually because they are not square matrices. By this trick, we achieve two goals. First, we minimize the computing time, moreover, and more importantly, we obtain a closed form expression which simplifies the estimation of the error on the SH coefficients, as we detail in the next section and in Appendix B. The elements of the vector $\boldsymbol{a}^{(\infty)}$ represent our best estimate ($\hat{a}_{\ell m}$) of the coefficients of the spherical harmonic decomposition $a_{\ell m}$.

C. Statistical measurement errors

In the following, we consider the SH coefficients $a_{\ell m}$ as a deterministic variable whose estimate,

$$\hat{a}_{\ell m} = a_{\ell m} + \epsilon_{\ell m}, \tag{24}$$

fluctuates due to measurement errors $\epsilon_{\ell m}$ induced by uncertainties in the reconstruction of η. The expectation over different observational measurements made on the same sample is thus $E[\hat{a}_{\ell m}] \equiv \langle \hat{a}_{\ell m} \rangle = a_{\ell m}$, i.e. we assume that the estimator provides an unbiased estimate of the coefficients of the spherical harmonic expansion.

The variance of the estimator is defined as

$$V[\hat{a}_{\ell m}] = V[\epsilon_{\ell m}] \equiv \sigma^2_{\ell m}, \tag{25}$$

and, in general, depends on both modes ℓ and m. An exact analytical expression for $\sigma_{\ell m}$ is far from trivial and unenlightening. It can be evaluated from the knowledge of the uncertainties in the distance modulus measurements [see Appendix B and cf. Eqs. (B1) and (23)].

An estimator of the power locked in each harmonic moment ℓ is the angular power spectrum [cf. Eq. (11)] estimator

$$\hat{\hat{C}}_\ell = \frac{1}{2\ell+1}\sum_{m=-\ell}^{\ell} |a_{\ell m} + \epsilon_{\ell m}|^2, \tag{26}$$

which can be expressed as

$$\hat{\hat{C}}_\ell = \frac{1}{2\ell+1}\sum_{n=0}^{2l} w_n^{(\ell)}, \tag{27}$$

where

$$w_n^{(\ell)} = \begin{cases} \hat{a}^2_{\ell 0} & n = 0 \\ 2\Re[\hat{a}_{\ell n}]^2 & \ell \geq n > 0 \\ 2\Im[\hat{a}_{\ell(n-\ell)}]^2 & 2\ell \geq n > \ell. \end{cases} \tag{28}$$

This decomposition is conveniently chosen to take into account that a_{l-m} and $a_{\ell m}$ are conjugate variables ($a_{\ell -m} = (-1)^m a^*_{\ell m}$). Thus, the variance of $\hat{\hat{C}}_\ell$ reads

$$V[\hat{\hat{C}}_\ell] = \left(\frac{1}{2\ell+1}\right)^2 \sum_{n=0}^{2\ell} V[w_n^{(\ell)}], \tag{29}$$

where

$$V[w_n^{(\ell)}] = \begin{cases} 2\sigma^4_{\ell 0} + 4\sigma^2_{\ell 0} a^2_{\ell 0} & n = 0 \\ 8\sigma^{(R)4}_{\ell n} + 16\sigma^{(R)2}_{\ell n}\Re[a_{\ell n}]^2 & \ell \geq n > 0 \\ 8\sigma^{(I)4}_{\ell(n-\ell)} + 16\sigma^{(I)2}_{\ell(n-\ell)}\Im[a_{\ell(n-\ell)}]^2 & 2l \geq n > \ell, \end{cases} \tag{30}$$

and where we have defined $\sigma^{(R)2}_{\ell m} = V[\Re[\hat{a}_{\ell m}]]$ and $\sigma^{(I)2}_{\ell m} = V[\Im[\hat{a}_{\ell m}]]$.

In Appendix C we show that the analytical estimates obtained using Eq. (29) provide a fairly good approximation to those obtained via a numerical Monte Carlo analysis (see the comparison in Table III). Expression (29) can be further simplified by making assumptions about the nature of the errors. If the distribution of the galaxies is isotropic and all of them have the same error in η ($\delta_i = \delta$), then the real and imaginary parts of $\hat{a}_{\ell m}$ are characterized by the same variance, and it will not depend on the considered harmonics ($\sigma^2_{\ell m} = \sigma^2 \approx \frac{4\pi}{N}\delta^2$), so

$$V[\hat{\hat{C}}_l] = \frac{2}{2\ell+1}[(\sigma^2 + \hat{C}_\ell)^2 - \hat{C}_l^2]. \tag{31}$$

The above formula neatly isolates the two quantities contributing to the observed variance: the error in the estimation of the distance modulus and the measured amplitude of the angular power spectrum $\hat{C}_\ell$.

Note, incidentally, that Eq. (31) differs from the expression that would be obtained by averaging over a statistical ensemble. Indeed, in this latter case $E_e[\hat{a}_{\ell m}] = 0$ (so $\hat{C}_\ell$ will be replaced by zero) and also $V_e[\hat{a}_{\ell m}] = C_\ell + \sigma^2$. It thus follows that the theoretical expression factoring in the contributions of cosmic variance is $V_e[\hat{\hat{C}}_\ell] = 2/(2\ell+1)(\sigma^2 + C_\ell)^2$, if, again, it is assumed that $\sigma_{\ell m}$ is isotropically distributed.

D. Systematic measurement errors

Equation (26) provides a biased estimate of the local value of the angular power spectrum $\hat{C}_\ell$ since its expectation over measurements is

$$E[\hat{\hat{C}}_\ell] = \hat{C}_\ell + \frac{1}{2\ell+1}\sum_{m=-\ell}^{\ell}\sigma^2_{\ell m}. \tag{32}$$

Measurement errors on the distance modulus lead to a systematic overestimation of the angular power spectrum $\hat{C}_\ell$, and the statistical bias term calculated in Eq. (32) might not fully remove the systematic shift. Indeed, expression (32) is strictly valid if the estimator $\hat{a}_{\ell m}$ [cf. Eq. (24)] is, as we assumed, affected only by statistical errors. It is true, however, that incompleteness and anisotropies in the sky distribution, as well as the pixelization and resolution strategy adopted to transform the discrete η observable into a field, could bias the $\hat{a}_{\ell m}$ estimator. Although any constant systematic term added in (24) does not affect the variance of the coefficients of $\hat{a}_{\ell m}$, it will result in an additional (and analytically nontrivial) term in Eq. (32).

The total systematic bias ΔC_ℓ affecting the estimator $\hat{\hat{C}}_\ell$ is thus more conveniently quantified using Monte Carlo simulations. The way Monte Carlo simulations are constructed and analyzed is discussed in Appendix C. There we also report the values of the systematic bias induced on the $\hat{C}_\ell$ estimates (see Table IV).

A different systematic error results from the SH decomposition of the logarithm of H_0 and not of H_0 itself. This choice of the observable, motivated by statistical reasons (cf. Sec. II), induces spurious higher order multipoles even if they are absent in H_0. This bias is however negligible. Indeed, in the ideal case in which $\tilde{H}_0$ is purely dipolar in nature $\tilde{H}_0/H_0 = (1 + \epsilon\cos(\alpha))$ (here ϵ is a small expansion parameter), one gets $\hat{C}_0 = 4\pi$, $\hat{C}_1 = \frac{4\pi}{9}\epsilon^2$ and $\hat{C}_\ell = 0$ for $l \geq 2$. The logarithmic transformation gives a new dipole power spectrum $\hat{C}_1 = \frac{4\pi}{9(\ln(10))^2}\epsilon^2 + o(\epsilon^4)$ and induces a parasitic quadrupole $\hat{C}_2 = \frac{4\pi}{225(\ln 10)^2}\epsilon^4 + o(\epsilon^6)$. Its amplitude is however negligible ($\frac{\hat{C}_2}{\hat{C}_1} \approx \frac{1}{25}\epsilon^2$), as it is that of the high order spurious multipole. This effect is thus largely subdominant (a factor roughly $\sim$30) compared to the typical errors that plague our analysis.

An additional effect that should in principle be considered is that, although we are not interested in the monopole of $\log\tilde{H}_0$ field, since we are not interested in calibrating the absolute scale of the Hubble constant, a redshift-dependent value of the parameter H_0 in Eq. (2) could lead to a spurious dipole component. This effect, which occurs if anisotropically distributed data are projected onto the sky and analyzed in two dimensions, does not affect the sample we analyze, for which the monopole amplitude appears to be fairly independent of redshift. Indeed, we have verified that $\langle\log\tilde{H}_0\rangle$ calculated at $z = 0.05$ and $z = 0.01$ changes by roughly 0.0006 (1.8628 ± 0.0010 and 1.8622 ± 0.0014 respectively for the CF3 sample) which corresponds to $\Delta H_0 \approx \Delta\eta H_0 \ln(10) = 0.1$ for $H_0 = 70$ km/s/Mpc) a negligible amount if compared to the errors affecting the analysis.

IV. DATA

Here we briefly describe the samples of redshift-independent distances used to estimate η.

A. The Pantheon sample

The Pantheon SNIa compilation [55] is comprised of 1048 objects lying in the interval $0.01 < z < 2.26$. The catalog was assembled using data from the Supernova Legacy Survey (SNLS) [56], the Sloan Digital Sky Survey (SDSS) [57,58], Pan-STARS1 (PS1) [55], [59–63] the Carnegie Supernova Project (CSP) [64] and various surveys made possible by the Hubble Space Telescope (HST), namely CANDLES/CLASH [65–67], GOODS [68] and SCP [69].

Although many previous investigations of kinematical anisotropies rely on the analysis of the full Pantheon sample, in this study we follow a pretty conservative approach and consider only a SNIa subsample with maximal spatial uniformity. To this end, we require the data to sample in a fairly isotropic manner the sky and also to display sufficient homogeneity in the radial coordinate.

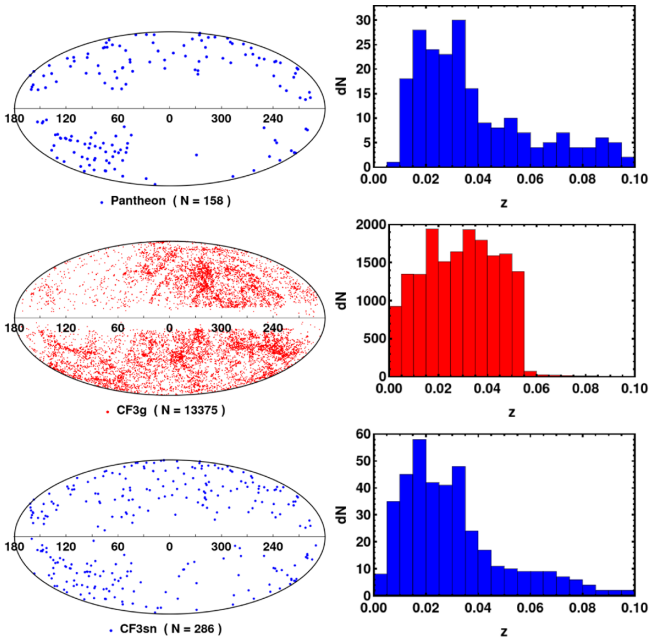

FIG. 2. Upper left: Mollweide projection, in galactic coordinates, of the distribution of the Pantheon SNIa with redshift $0.01 < z < 0.05$. Upper right: histograms of the number of counts as a function of redshift. The second and the third rows are the same as the first, but for the CF3g and CF3sn samples respectively.

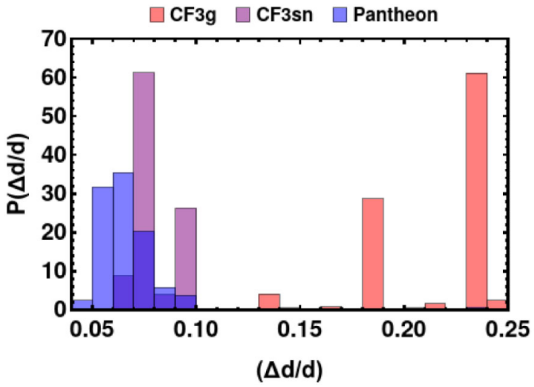

FIG. 3. The probability distribution of the relative error in the distances ($\Delta d/d \approx \Delta\mu \ln 10/5$) measured in samples CF3g, CF3sn and Pantheon in the interval $0.01 < z < 0.05$.

The goal is to minimize possible biases and systematic effects induced by incomplete spatial sampling without sensibly reducing the statistical constraining power of the data.

In Fig. 2 (the first row) the angular distribution of the Pantheon data is shown together with the differential number counts profile $dN(z)$ as a function of redshift. There are no objects in the very local patch of the universe, below $z = 0.01$, and the sample becomes quickly anisotropic as soon as the redshift is larger than $z = 0.05$. It also becomes inhomogeneous, i.e. the scaling of dN is not anymore proportional to z^2, for $z \gtrsim 0.04$. As a consequence, a trade-off threshold value $z = 0.05$ is chosen for selecting the SNIa sample to be used in this study. This leaves us with a subsample containing 158 SNIa.

B. The Cosmicflows-3 data

For the purposes of our analysis, we complement the Pantheon supernovae sample with the Cosmicflows-3 catalog [70]. This is an all-sky galaxy catalog comprised of 17669 nearby galaxies $z \leq 0.116$ for which redshift-independent distances are inferred using the correlation between galaxy rotation and luminosity (Tully-Fisher law), or the Fundamental Plane methods.

This galaxy catalog offers three key advantages: a completely independent way of estimating galaxy distances and a richer collection of distance moduli μ (nearly 100 times more than those contained in the supernovae catalog). It is this large statistical figure that helps beating down the large error with which the individual galaxy distances are estimated. These uncertainties are shown in Fig. 3, where they are also compared to the typical inaccuracies that characterize the SNIa distances. The latter are at least a factor of 2 smaller than those based on the Tully-Fisher or the Fundamental Plane estimates (so each is 4 times or more valuable in a statistical weighting scheme). An additional benefit is that the association of galaxies to groups allows local nonlinear contributions to the observed redshift to be averaged away. In this way, the redshift is less sensitive to the local gravitational field at submegaparsec scales and more directly reflects the large-scale properties of spacetime.

The angular and radial distribution of the Cosmicflows-3 galaxies is shown in Fig. 2 (the second and the third rows). They are fairly evenly distributed in both redshift and position in the sky except for redshifts greater than 0.05. So, we do not include the galaxies beyond this redshift since the sample becomes too sparse and covers the sky anisotropically. We also exclude from the sample, galaxies with redshift less than 0.01, in order to facilitate the comparison with the results obtained from the Pantheon data. We, therefore, focus our analysis on the Cosmicflows-3 subsample which is constrained in the range $0.01 < z < 0.05$ and includes 13661 galaxies. We add in this respect that the purpose of our analysis is to obtain a coarse-grained description of the expansion rate. In the periphery of the Local Group, the geometry and dynamics of the metric are instead dominated by a few large nonlinear structures, and, as a consequence, the galaxies poorly track the large-scale gravitational field we are interested in.

Within this redshift range, the CF3 catalog contains 286 galaxies hosting a SNIa (Fig. 2, third row) for which the distance modulus is known using the standard candle method. Although systematically homogenized, this compilation of SNIa-based distances remains fundamentally

heterogeneous, with distance moduli derived from different light curve fitters. Although this dataset contains the Pantheon as a subsample, we use it as a control sample to check the robustness of the results we obtain using the Pantheon dataset alone. In what follows, we will refer to the CF3 subsample with SNIa-based distances as CF3sn and indicate the complementary set with the acronym CF3g.

V. RESULTS

In this section, we present and comment on the results obtained by applying the formalism to various datasets. The relevant parameters of the SH analysis of the expansion rate field are quoted in Table I. Note that for each entry in this table we do not report the bare value returned by the spherical harmonic estimator, but that obtained after subtracting the systematic bias factors quoted in Table IV of Appendix C. The quoted statistical uncertainties are those estimated numerically by means of 1000 Monte Carlo simulations, although, as we have highlighted in the previous section, analytical estimations are effectively comparable (see Table III in Appendix C).

Figure 4 shows the η field for the CF3 sample tessellated according to different resolutions (192, 48 and 12 pixels). Smoothing mainly affects the errors with which the relevant SH parameters are estimated, with the error generally decreasing as the number of pixels decreases (as judged on the basis of systematic and statistical errors determined by Monte Carlo simulations, see Tables IV and III in Appendix C). The central values of the SH parameter, instead, are statistically stable: they fluctuate from one reconstruction to the next, but the discrepancies are within what is expected from a random sampling of a common underlying Gaussian distribution. The results are thus globally independent of the pixelization strategy adopted.

However, a valid pixelization scheme for one sample may not be suitable for reconstructing the signal in another catalog. A 48-pixel smoothing is for example less than optimal for sizing even the dipole of the sparse SNIa sample. Only when the analysis is performed by tessellating the sky at lower resolution (12 pixels) we can unpack the information contained in the lowest multipoles. The price to pay is that now the higher multipoles cannot be estimated: already the multipole $\ell = 3$ becomes now too noisy and therefore unresolved.

The strongest contribution to the signal is provided by the dipole term, whose maximal intensity is about 1% of the signal locked in the normalizing term $\log H_0$, i.e. ∼4.5% of H_0. The power locked in the dipole (as determined using the CF3g sample) is $\hat{C}_1 = (4.0 \pm 0.6) \times 10^{-4}$, an estimation characterized by a high signal-to-noise ratio (snr ∼ 6.6). Consistently, this value is in excellent agreement (well within 1σ) with that estimated from both the CF3sn and the Pantheon sample ($(3.7 \pm 1.5) \times 10^{-4}$ and $(3.5 \pm 2.7) \times 10^{-4}$ respectively).

Due to the increased statistical power, the angular position of the dipolar anisotropy axis is better resolved when the whole CF3 sample is analyzed ($l_d = 285 \pm 5$, $b_d = 11 \pm 4$). The 95% confidence level (CL) uncertainty region falls within the 68% CL uncertainty region defined by any one of the SNIa samples. We remark that this direction is not far away from that of the Shapley Concentration which also roughly coincides with that of the Great Attractor [71]. We will further develop the physical implications of this preferential axis when we discuss bulk flows in Sec. V B.

We then ask whether this long-range dipole correlation found in each data sample is statistically significant. To answer the question we compare our hypothesis (occurrence of a truly physical anisotropic dipole) against the probability of the occurrence of a dipole, as a statistical fluctuation, in a model where the fluctuations in H_0 are uncorrelated. To this end, we perform Monte Carlo simulations to reconstruct the p-value statistics to invalidate our null hypothesis against observed data. Specifically, we consider a model of the expansion rate fluctuation η that contains only the monopole and no higher order terms and generate 10000 Monte Carlo mock catalogs simulating each dataset. This is done by replacing the model distances with a fictitious one randomly drawn from a Gaussian distribution $G(\eta, \sigma_\eta)$, where σ_η is the observational error quoted for each object in the various data samples. For each simulation, we calculate the power in the resulting dipole ($\hat{C}_1^{\rm sim}$) and compare it with the observed one $\hat{C}_1^{\rm obs}$. We then estimate the frequency p with which $\hat{C}_1^{\rm sim} > \hat{C}_1^{\rm obs}$. A standard rule of thumb consists in rejecting the null hypothesis, i.e. refute the statistical significance of the signal we observe, if $p > 5\%$. On the contrary, we find that p is virtually zero i.e. $p < 10^{-4}$ for CF3g and also critically low $p = 0.3\%$ and 4.4% for CF3sn and the Pantheon sample respectively (see Table I), thus confirming the nonaccidental nature of the dipolar anisotropy.

We further note that the dipole in the expansion rate fluctuations is consistently tracked by the various samples of galaxies and supernovae. Its intensity and direction agree fairly well and fluctuations from one catalog to the next are within what is expected from a random sampling of a common underlying value. Since the distances and the associated measurement errors are reconstructed using different and independent methods and calibrations for galaxies and supernovae, it is difficult to interpret these signals as simple statistical fluctuations and to relegate this coincidence to the role of a fluke. These results, on the contrary, seem to suggest that both the galaxy sample and the SNIa sample trace the same anisotropic background expansion rate, despite differences in the uncertainties with which the distance moduli are determined and in the sampling frequency of large-scale structures.

We find that the contribution of the quadrupole component to the anisotropies observed in the η expansion field is significant both in terms of its amplitude, which is

TABLE I. Parameters of the spherical harmonic decomposition. Central values are not the bare value returned by the spherical harmonic estimator but are obtained after subtracting the systematic effect determined by means of 1000 Monte Carlo simulations (the bias factors given in Table IV (see Appendix C). Statistical errors are also determined using Monte Carlo simulations (see Table III in Appendix C). We quote also the direction for the dipole, and direction of the peaks of the $\ell = 2$ and 3 multipoles which are close to the direction of the dipole. The p-value is computed by using 10000 Monte Carlo simulations. For Pantheon, the error in the direction of the quadrupole is not quoted because it is larger than 180 degrees.

Sample	$N_{\rm pix}$	l_d	b_d	$\hat{C}_1$ (10^{-4})	$\frac{\eta_{1\rm max}-\lvert\eta_{1\rm min}\rvert}{2}$ (10^{-2})	p-value (%)	l_q	b_q	$\hat{C}_2$ (10^{-4})	$\frac{\eta_{2\rm max}-\lvert\eta_{2\rm min}\rvert}{2}$ (10^{-2})	p-value (%)	l_t	b_t	$\hat{C}_3$ (10^{-4})	$\frac{\eta_{3\rm max}-\lvert\eta_{3\rm min}\rvert}{2}$ (10^{-2})	p-value (%)
CF3 [0.01, 0.05]	192	291 ± 15	12 ± 7	3.0 ± 1.6	1.6	0.03	323 ± 16	9 ± 4	2.4 ± 0.9	1.9	0.12	289 ± 24	16 ± 15	0.1 ± 0.4	1.2	30.44
CF3 [0.01, 0.05]	48	283 ± 6	12 ± 5	5.3 ± 0.8	1.9	< 0.01	310 ± 11	4 ± 8	0.9 ± 0.3	1.1	< 0.01	284 ± 7	12 ± 5	0.5 ± 0.2	1.3	0.01
CF3g [0.01, 0.05]	48	286 ± 7	4 ± 6	7.0 ± 1.0	2.0	< 0.01	338 ± 8	22 ± 5	1.1 ± 0.4	1.3	< 0.01	255 ± 9	11 ± 5	0.7 ± 0.2	1.5	0.01
CF3 [0.01, 0.05]	12	285 ± 5	11 ± 4	5.1 ± 0.8	1.9	< 0.01	308 ± 7	1 ± 7	1 ± 0.3	1.1	< 0.01	...	...	...	...	...
CF3g [0.01, 0.05]	12	296 ± 6	18 ± 5	4.0 ± 0.6	1.7	< 0.01	323 ± 34	2 ± 17	1.3 ± 0.4	1.4	< 0.01	...	...	...	...	...
CF3sn [0.01, 0.05]	12	322 ± 23	-8 ± 18	3.7 ± 1.5	1.5	0.27	343 ± 15	-8 ± 10	1.7 ± 1.4	1.7	2.90	...	...	...	...	...
Pantheon [0.01, 0.05]	12	334 ± 42	6 ± 20	3.5 ± 2.7	1.6	4.37	337	-5	0.6 ± 1.9	1.6	33.33	...	...	...	...	...
CF3 [0.01, 0.03]	12	279 ± 5	12 ± 5	7.8 ± 1.0	2.3	< 0.01	310 ± 8	11 ± 6	2.9 ± 0.6	1.9	< 0.01	...	...	...	...	...
CF3 [0.03, 0.05]	12	301 ± 15	10 ± 14	1.1 ± 0.7	1.0	0.03	277 ± 28	-12 ± 11	0.9 ± 0.3	1.0	2.04	...	...	...	...	...

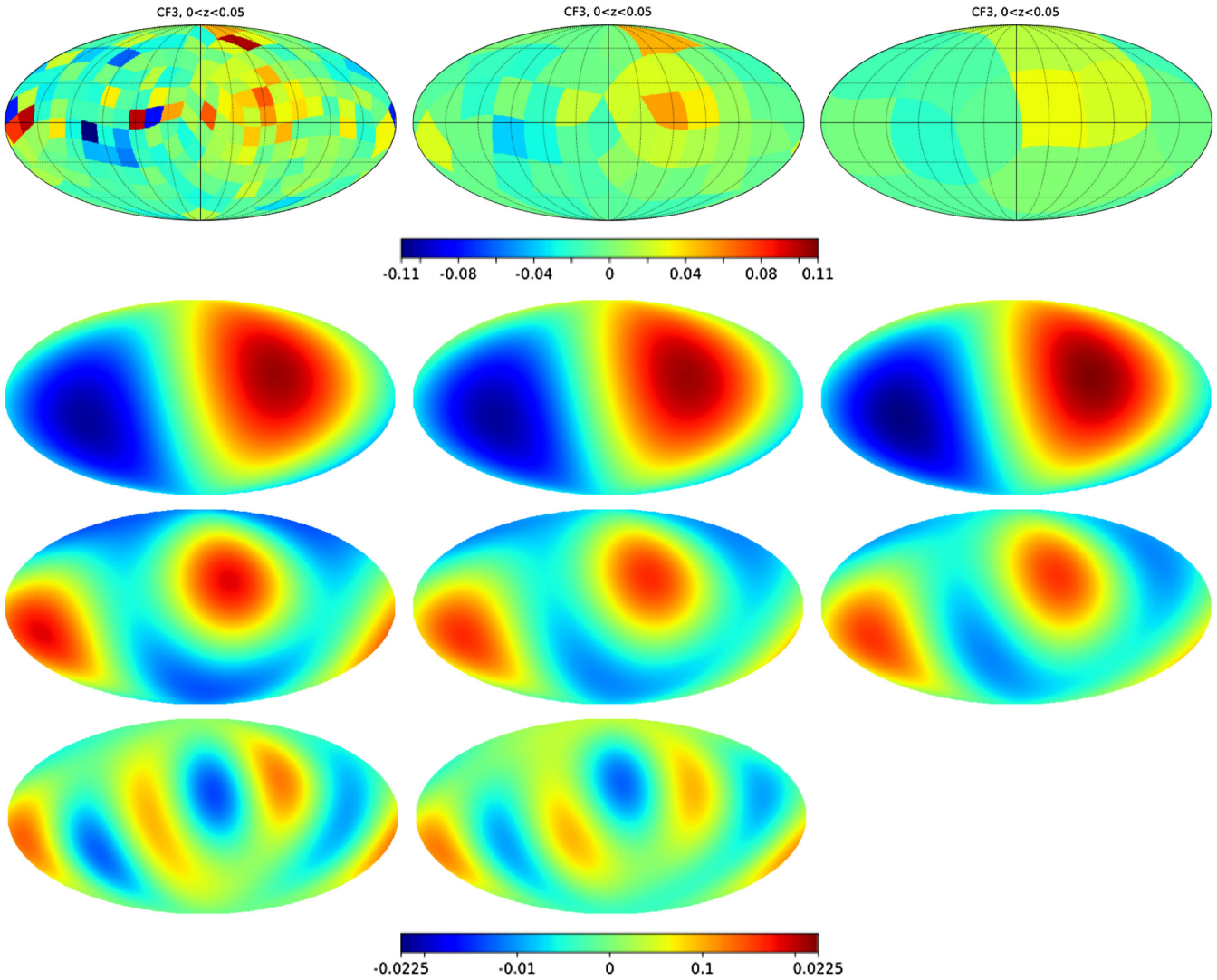

FIG. 4. Upper panel: the angular η field traced by the CF3. From left to right are shown different resolution maps corresponding to the tessellation of the sky with 192, 48 and 12 HEALPIX cells. The dipole η_1 (second panel from the top), quadrupole η_2 (third panel from the top), and octupole η_3 (bottom panel) components are also shown.

comparable to that of the dipole [$\max(\eta_2) \sim \max(\eta_1)$], and in terms of its statistical significance measured by the signal-to-noise ratio (snr ~ 3.25 for CF3g and snr ~ 1.2 for CF3sn). Again, a p-value analysis of its significance performed simulating 1000 mock catalogs still confirms that the chances of this signal being a statistical artifact are minimal (the probability of reconstructing a quadrupole larger than the observed one due to a random fluctuation is effectively zero for CF3g and smaller than 3.3% for CF3sn). The probability is reduced even more dramatically if the test is run to answer the question; what is the likelihood of finding a dipole and quadrupole of similar intensity to that observed in the case where the underlying expansion field is uniform? This result, both independently and in combination with what was found for the dipole term, confirms that the probability of the observed anisotropy being a statistical artifact is very small.

More intriguingly we find that the maximum of the quadrupole signal is aligned with the dipole direction (see Fig. 4). This peculiar alignment is consistently and independently confirmed by both galaxy (CF3g) and SNIa (CF3sn) samples (see Fig. 5 and Table I).

We highlight the fact that inferences made with the different samples are consistent, but there is one difference that deserves attention and further investigation: there is no evidence of a quadrupole component in the Pantheon data as judged from the amplitude of the $\hat{C}_2$ power, both in terms of its snr and of its p-value. This result confirms a similar null detection obtained by [47] although in a different redshift range and using an alternative method which is not based on the Fourier decomposition of the signal but on the maximum likelihood adjustment of quadrupolar coefficients. The possible reasons for this lack of signal will be analysed in Sec. V A.

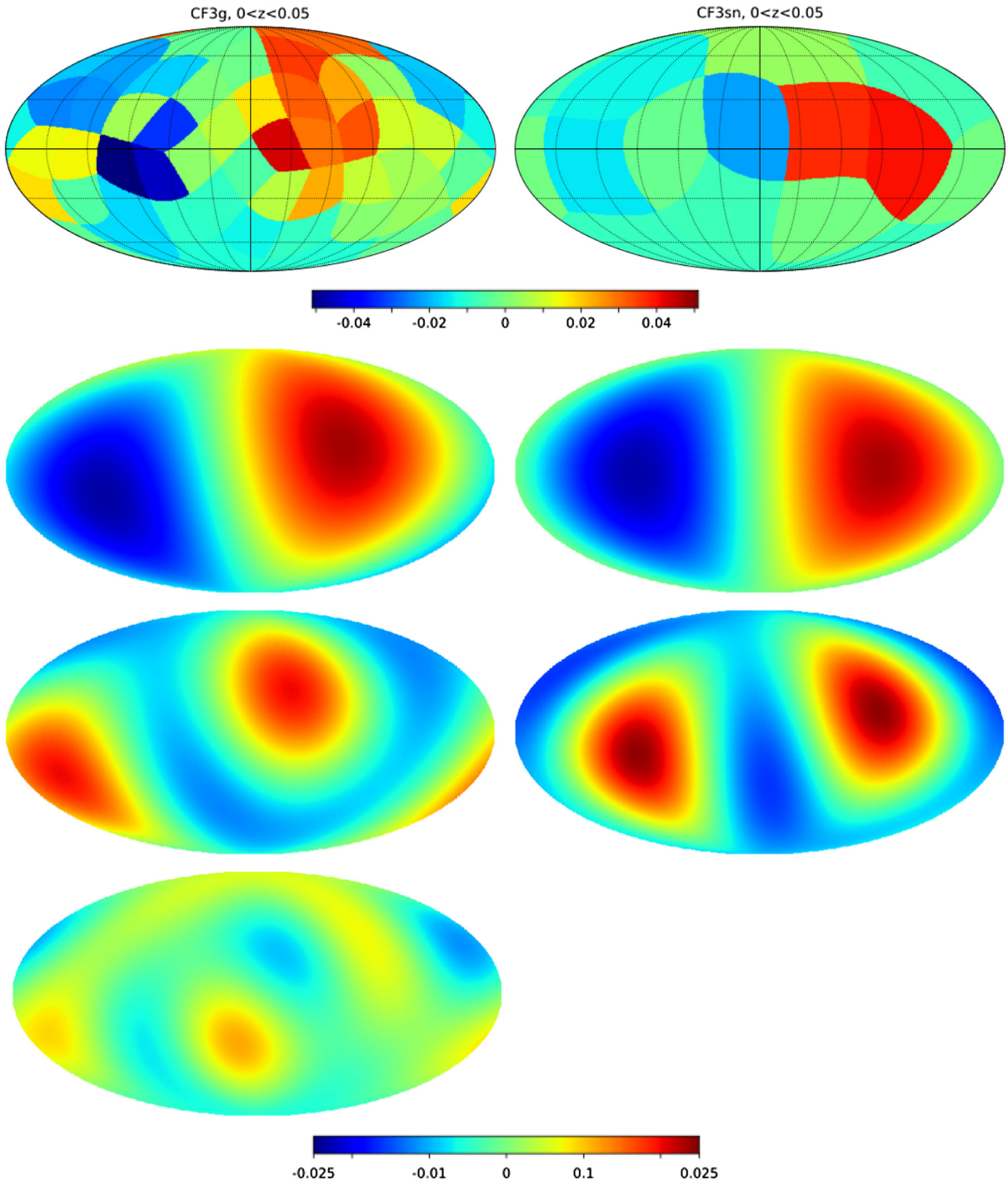

FIG. 5. Left panel: the η field tessellated into 48 pixels and traced by the CF3g sample. The dipole η_1 (second panel from the top), quadrupole η_2 (third panel from the top), and octupole η_3 (bottom panel) components are also shown. Right panel: same as above, but now the expansion rate fluctuation field is tessellated into 12 pixels and traced by the CF3sn sample.

Interestingly, we find evidence (snr ~ 2.5) that the contribution of the octupole is also not negligible, at least when the whole CF3 sample is analyzed with a 48 HEALPIX pixel smoothing. The power stocked in this component is roughly half that in the quadrupole although the intensity peaks at a value comparable to the maximum intensity of the quadrupole. Even more unexpected is the fact that the direction of the maximum of the octupole component ($l_t = 284 \pm 7$, $b_t = 12 \pm 5$) appears to be aligned with that of the dipole ($l_d = 283 \pm 6$, $b_d = 12 \pm 5$) and of the quadrupole ($l_q = 310 \pm 11$, $b_q = 4 \pm 8$) (see Table I).

The fact that we cannot confirm the octupolar signal independently in the 192 and 48 pixels maps suggests the need to pursue another route to quantify its amplitude and

direction, and also to ensure the general robustness of our results. We have thus determined the value of the SH parameters (direction of the dipole and power spectrum coefficients) not by Fourier calculating them via Eq. (23) but by considering them as free fitting parameters to be determined by means of a maximum likelihood analysis. In the ideal case of zero noise, the best approximation theorem ensures that the Fourier coefficients are also those that minimize the difference (in the L2 norm) between the signal and its decomposition on a finite orthonormal basis. This statistical approach is independent from any tessellation scheme adopted to convert the estimator of η [cf. Eq. (4)] into a stochastic field. Indeed, we directly minimize the difference between the discrete random variable $\hat{\eta}(\mathbf{r})$ and the SH model (7). In the presence of errors, however, it does not protect against power spilling in and out from multipolar coefficients of different orders. The method and results are detailed in Appendix C (see Tables V and VI where we quote the least-square best fitting amplitudes together with the 68% CL)

Overall, the central values and errors deduced by means of this statistical procedure are in excellent agreement with the Fourier determinations reported in Table I and provide independent confirmation of the soundness of our findings. Interestingly, the detection of the octupolar component is confirmed, at least for the whole CF3 sample. The best fitting amplitude $\hat{C}_3^{\rm fit} = 0.6 \pm 0.2$ is consistent with what is determined by the Fourier analysis ($\hat{C}_3 = 0.5 \pm 0.2$), and

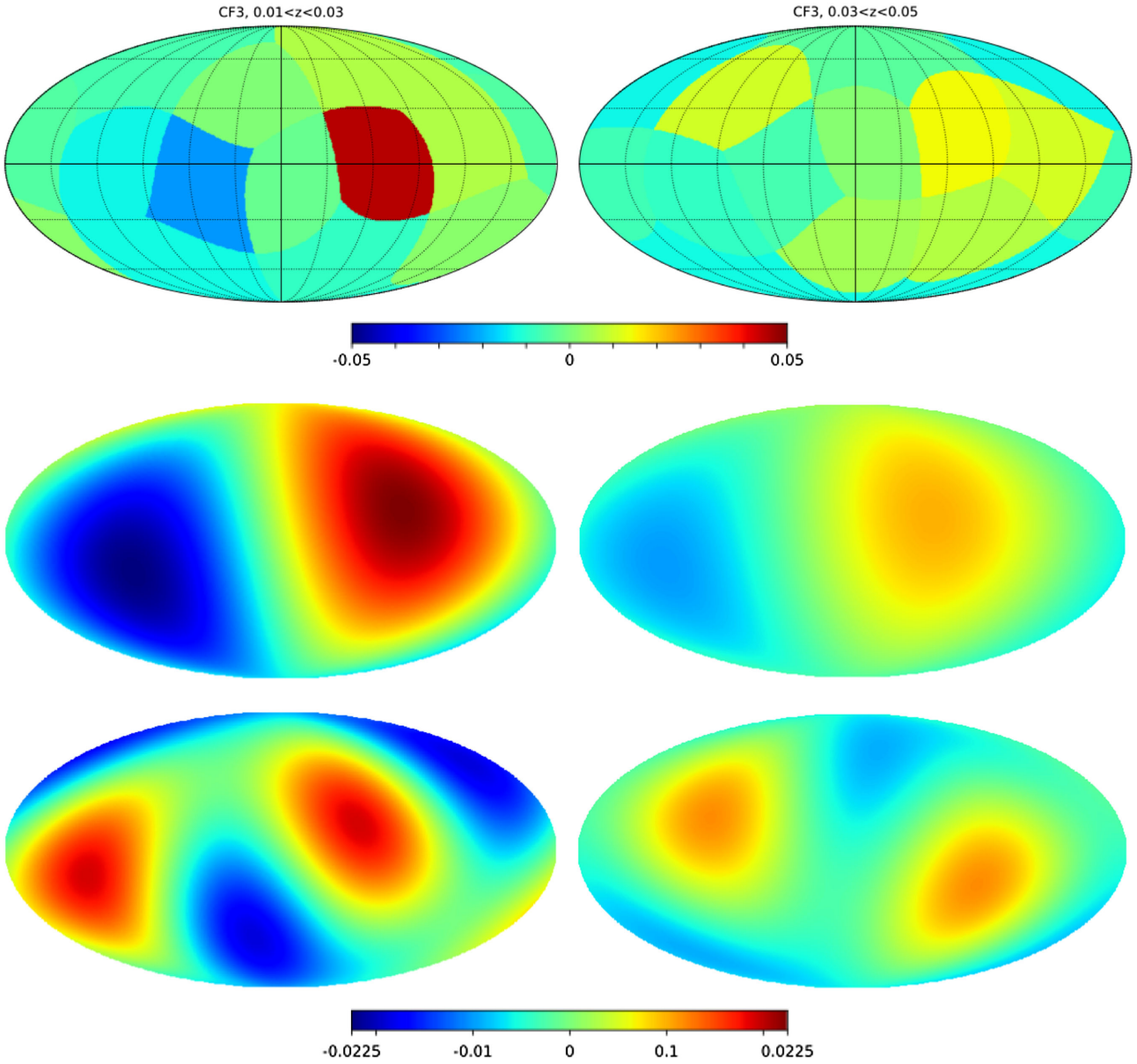

FIG. 6. Left panels: the η field (upper), its dipolar (center) and quadrupolar (lower) components traced by the CF3 sample in the redshift interval $0.01 \leq z \leq 0.03$. Right panels; the same as before but for galaxies in the deeper redshift range $0.03 \leq z \leq 0.05$.

also the direction of the axis of maximum intensity is in the general direction of the dipole ($l \sim 287, b \sim 9$). Also the minimum value of the normalized χ^2 statistic is of relevance. This implies that the 2D model (7) provides an adequate fit to data that depends, in principle, on the 3D spatial position. This fact further supports our claim on the validity, in the limit $z \ll 1$, of the ansatz (1).

The advantage of a SH analysis of anisotropies over other approaches is that the fact that Fourier coefficients represent projections on an orthonormal basis implies that adding additional higher order terms to the SH expansion does not alter the characteristics (amplitude and direction) of the low-order components. It is however critical to assess whether their curious structure is the result of a fortuitous averaging coincidence, i.e. the accidental combination of different patterns at different depths, or it is a persistent feature independent from the radial depth of the survey.

To investigate this issue we repeat the analysis separately in two redshift intervals $0.01 \leq z \leq 0.03$ and $0.03 \leq z \leq 0.5$. These are the smallest subvolumes that still provide detections with acceptable *snr* and low risk of misinterpretation (low p-value), if only for the CF3 sample. Results are shown in Fig. 6.

The direction of the dipole and the quadrupole reconstructed in the two volumes consistently point in the same direction (to within about 1σ) and is also in excellent agreement with the results found for the whole samples. This confirms that the alignment phenomenon is not a random overlap but rather physical in nature. There is, instead, a significant change in the power spectrum amplitude of the multipoles. The $\hat{C}_1$ component decreases by more than about 5.5σ as the redshift of the sample doubles. The same decrement with depth ($\sim 3\sigma$) is observed for the amplitude of the $\hat{C}_2$ coefficient.

As a further check, we investigated whether quadrupole or octupole components are spuriously generated by the anisotropic and inhomogeneous distribution of galaxies and supernovae. To this end, we simulate an expansion rate fluctuation field that has a dipole component of the same intensity as that detected by the data, but with zero quadrupole and octupole. We then perturb the model's redshift-independent distances by adding Gaussian noise that mimics observational errors. Finally, we apply the SH analysis pipeline and examine the detection rate of a quadrupole or octupole of the same intensity as those measured from the real data. The power in both channels ($\hat{C}_2$ and $\hat{C}_3$) is on average an order of magnitude lower than that inferred from the CF3 dataset. For example, 10000 Monte Carlo replicas of the CF3 sample, analyzed with a smoothing of 48 pixels, give, on average, $\hat{C}_2 = 0.1 \pm 0.1$ and $\hat{C}_3 = 0.09 \pm 0.06$. Moreover, the probability of simulated values even more extreme than those actually observed is effectively zero ($p < 10^{-4}$). Furthermore, if a dipole and a quadrupole of the same amplitude as the measured ones are inserted into the $\tilde{H}_0$ map itself, instead of η, we find that the systematic and statistical errors as determined by the analysis of the Monte Carlo simulations induce on average a signal $\hat{C}_3 = 0.1 \pm 0.06$. Also the p-value for an even more extreme octupole than the one measured is negligible ($p = 0.01\%$).

A. Axial symmetry of the multipoles

In Fig. 7 we show the 3D structure of the quadrupole component of the expansion rate fluctuations η reconstructed using either the galaxy or the supernovae sample. This figure offers a different perspective on the dipole-quadrupole alignment. It shows that both quadrupoles independently reconstructed using galaxy and supernova data present an axially symmetric configuration which strongly polarizes in the direction defined by the dipole.

This additional symmetry, although physically unexpected since it seems to imply extreme fine-tuning in the local distribution of matter fluctuations, makes it possible to simplify, at least mathematically, the analysis of the anisotropies of the eta field. The fact that the direction (l_d, b_d) along which the multipoles align (Apex direction) defines not only a preferred axis, but indeed an axis of symmetry implies that the expansion rate fluctuation field η effectively depends only on a single variable, the polar

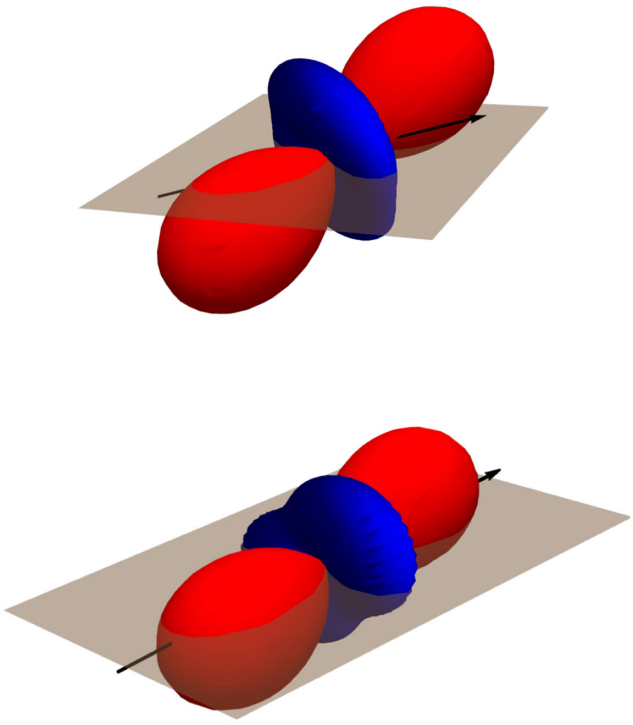

FIG. 7. The 3D structure of the multipole component η_2 of the CF3g sample (upper panel) and for the CF3sn sample (lower panel). The radial coordinate represents the absolute value for η; the red and blue colors indicate positive and negative signs respectively. For reference, the gray surface represents the orientation of the galactic plane while the black arrow gives the direction of the dipole as reconstructed for each sample.

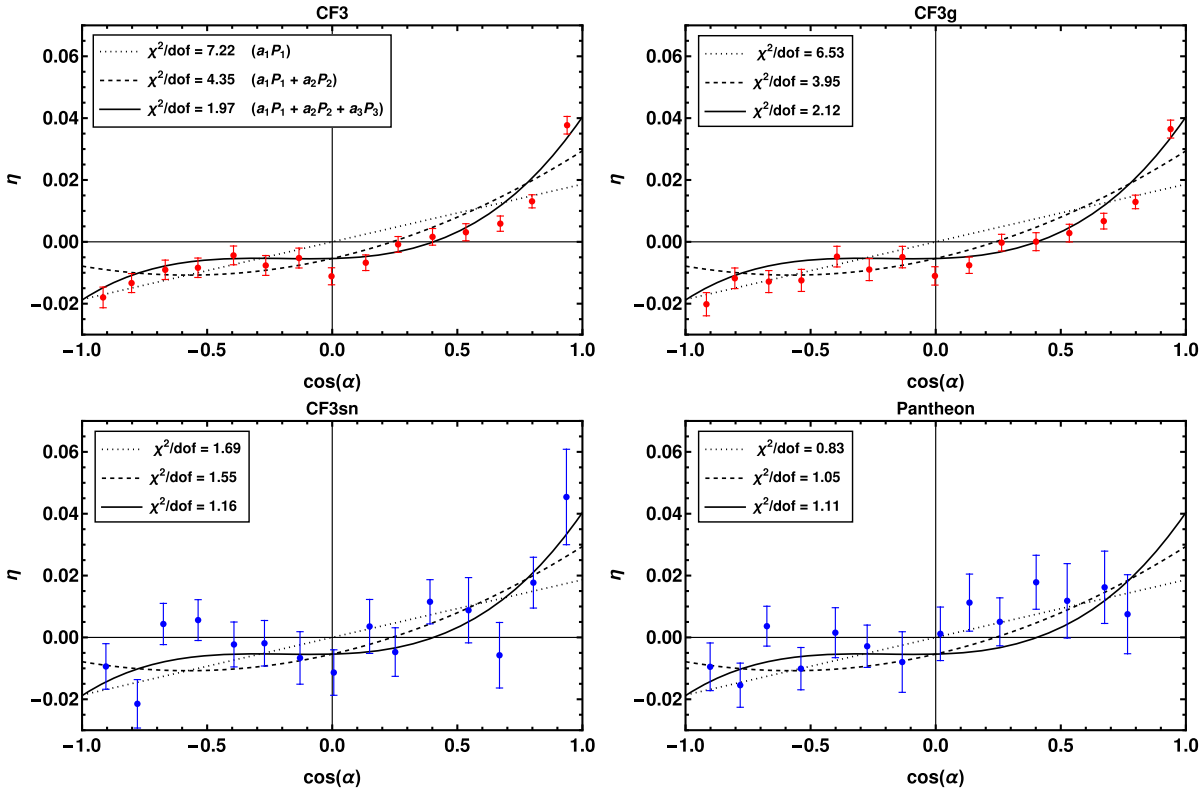

FIG. 8. Upper left: average value of η, for the CF3 sample, in open spherical sectors of identical width $\Delta\cos\alpha = 2/15$ and angular separation α from the direction $l = 285$, $b = 11$. The dotted line corresponds to the dipolar model ($a_1 = 1.9 \times 10^{-2}$), the dashed line includes also the contribution of a quadrupole term ($a_2 = 1.1 \times 10^{-2}$). The effects of adding the octupole term ($a_3 = 1.1 \times 10^{-2}$) are shown by the solid line. These models are compared to CF3g data (upper right), the CF3sn data (lower right) and the Pantheon data (lower right). In this latter case, note the absence of data in the rightmost bin, i.e. along the direction in which the low-order multipoles of the CF3 sample align.

angle α between between the line of sight of an object and the direction (l_d, b_d). A simple expansion of the field in Legendre polynomials $P_\ell(\cos\alpha)$, as opposed to the full spherical harmonics machinery, is thus enough for seizing the essential functional behavior of the η field.

The average value $\eta(\alpha)$ reconstructed in open spherical sectors of identical width having the center on the axis of symmetry and angular separation α from the apex direction is shown in Figs. 8 and 9 for the galaxy and SNIa samples. The Fourier coefficients of the expansion,

$$\eta(\alpha) = \sum_{\ell=1}^{3} a_\ell P_\ell(\cos\alpha), \tag{33}$$

are computed as

$$a_\ell = \frac{2\ell+1}{N_{\rm bins}} \sum_{i=1}^{N_{\rm bins}} \eta(\alpha_i) P_\ell(\cos\alpha_i), \tag{34}$$

and the results are quoted in Table II. Again, since the Legendre basis is orthogonal, the inclusion of the higher moments does not modify the value already calculated for the lower order terms. As a check of the stability of the estimation, we have also calculated the Legendre coefficients as $a_\ell = \sqrt{\frac{2\ell+1}{4\pi}} a_{\ell 0}$, where the coefficient $a_{\ell 0}$ is the SH component [cf. Eq. (9)] reconstructed after rotating the z axis into the position defined by the symmetry axis. We find that the results from the two methods are effectively indistinguishable.

The first thing we remark on is that the coefficients computed for different samples are all compatible among themselves, within 1-σ uncertainty. For this reason, the data from various samples shown in Figs. 8 and 9 are compared to the best-reconstructed template, the one with smaller errors, i.e. that resulting from the analysis of the whole CF3 sample. This helps in judging the consistency of different datasets in tracing the same underlying expansion rate fluctuation field. Concerning the contributions to the signal, we see that the dipole term alone, as expected, on the basis of the results of the previous section provides a poor description of the angular modulation of η. This is true for both the CF3g and CF3sn samples. An analysis of the goodness of fit with a reduced χ^2 statistic gives 6.55 and 1.57 respectively, i.e. a probability $p \sim 0$ and $p \sim 7\%$

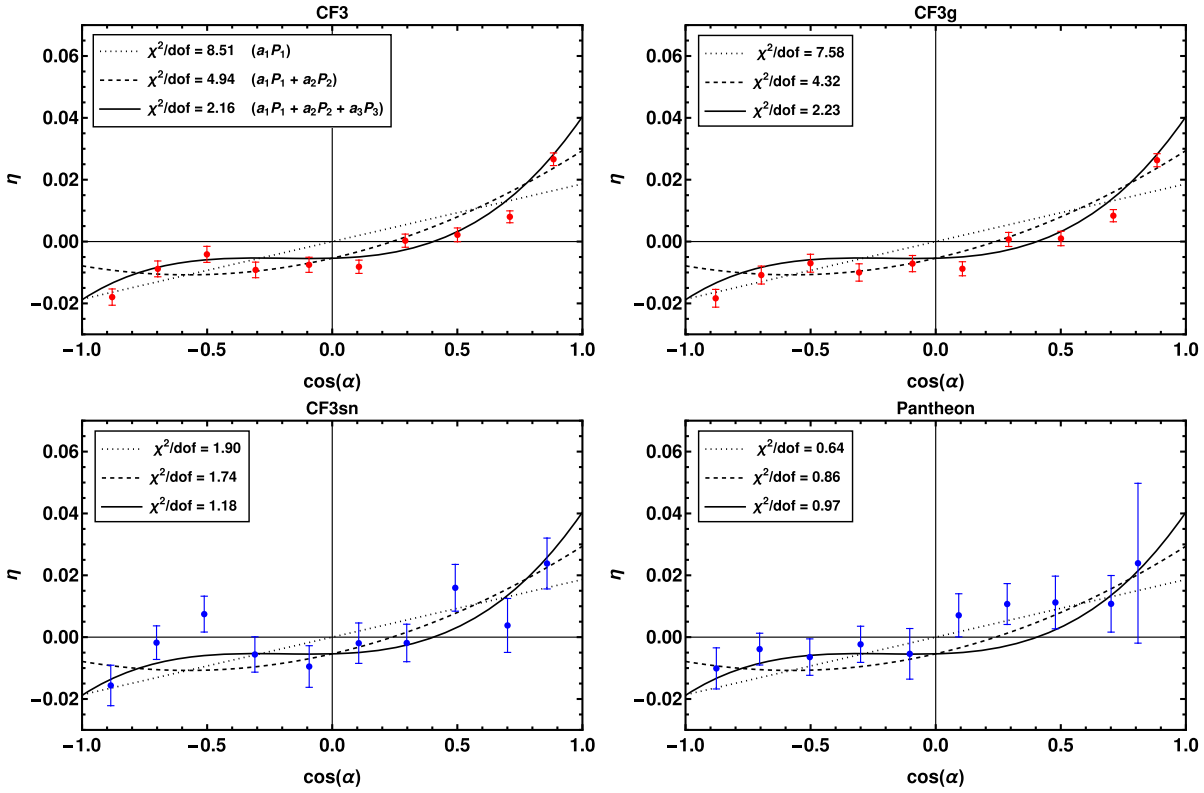

FIG. 9. The same as Fig. 8, with the same curves, but the number of bins is 10 here.

respectively of being wrong in rejecting the dipolar model. Although the latter value is formally higher than the traditional rejection threshold of 5%, and thus the risk of rejecting a good model is not negligible, it is equally true that once the quadrupole and octupole terms calculated for the CF3 sample are added to the model, the description of the CF3sn data improves, as evidenced by the systematic decrease in the χ^2 statistic.

As already discussed in Sec. V the Pantheon sample provides an exception, in that it does not show sign of a quadrupolar or higher order multipole components. A simple dipole optimally captures the angular modulation of the fluctuations of the expansion rate η ($\chi^2/\mathrm{dof} = 0.66$). Moreover, by including the quadrupole and octupole terms, the goodness of fit systematically degrades. The lack of signal is explained by the concomitance of two effects: the

TABLE II. The coefficient of Legendre expansion for 15 and 10 bins in $\cos\alpha$ where α is the angle between the open spherical sectors and the apex direction $(l, b) = (285, 11)$. The error is calculated by the error of average η for each bin. a_ℓ is calculated by Eq. (34).

Sample	N_{bins}	a_1 (10^{-2})	a_2 (10^{-2})	a_3 (10^{-2})	χ_1^2/dof	χ_2^2/dof	χ_3^2/dof	v_b (km/s)
CF3 $0.01 < z < 0.05$	15	1.9 ± 0.1	1.1 ± 0.2	1.1 ± 0.2	7.22	4.35	1.97	318 ± 22
CF3g $0.01 < z < 0.05$	15	2.0 ± 0.1	1.0 ± 0.2	1.0 ± 0.2	6.55	4.07	2.23	334 ± 24
CF3sn $0.01 < z < 0.05$	15	1.7 ± 0.4	1.2 ± 0.6	1.4 ± 0.6	1.57	1.48	1.10	244 ± 64
CF3 $0.01 < z < 0.05$	10	1.7 ± 0.1	0.9 ± 0.2	0.6 ± 0.2	8.50	4.83	2.71	292 ± 21
CF3g $0.01 < z < 0.05$	10	1.8 ± 0.1	0.9 ± 0.2	0.5 ± 0.2	7.59	4.34	2.83	307 ± 23
CF3sn $0.01 < z < 0.05$	10	1.3 ± 0.4	0.5 ± 0.5	0.4 ± 0.5	1.53	1.40	1.18	195 ± 57
Pantheon $0.01 < z < 0.05$	10	1.6 ± 0.7	0.1 ± 0.7	-0.8 ± 0.5	0.46	0.46	0.54	243 ± 110

larger error bars with which the η observable is reconstructed from the sparse Pantheon sample and also, importantly given the alignment between the dipole and quadrupole found in the CF3g and CF3sn samples, the lack of objects along such a critical direction in the Pantheon sample.

B. Bulk motion model

The perturbation theory of the standard cosmological model provides a framework for interpreting our results. If peculiar velocity is random and uncorrelated in a given angular direction, the average expansion field η vanishes in that direction. Consider instead a peculiar velocity field v_b which is constant in both direction and amplitude over a typical scale R. If we choose α as measuring the angle between its direction and the line of sight, the expansion field is predicted to vary as [cf. Eq. (6)]

$$\eta(\alpha) = \frac{v_b}{\ln 10}\langle (1+z)/z \rangle \cos\alpha. \tag{35}$$

Suppose that $\langle (1+z)/z \rangle$, the average over the volume subtended by circular bands of angular separation α from the direction of the bulk motion, does not depend on α, which is a fairly good approximation for large samples. Then, by comparing (35) with (33), we deduce that the bidimensional expansion field η is compatible with being the sky projected realization of a three-dimensional bulk flow model. The amplitude of the bulk velocity follows from the amplitude of the dipolar parameter a_1 (the coefficient of the expansion on the Legendre basis P_1):

$$v_b = \frac{a_1 \ln 10}{\langle (1+z)/z \rangle}. \tag{36}$$

Assuming 500 km/s as a typical value for the peculiar velocity of galaxies, we expect the latter relation to apply fairly well for objects with $z \geq 0.01$, those considered in our analysis. Note that in this picture, the amplitude of the bulk is controlled by the amplitude of the dipolar parameter a_1 and also by the depth of the survey volume.

The direction of the bulk motion for the three samples is shown in Fig. 10. This direction results from separating in the SH analysis the direction of the dipole from that of other higher order multipoles. However, due to the alignment of the lower multipoles, the direction of the bulk coincides fairly well with the direction of maximum anisotropy in the η maps.

It is interesting to note that the direction of the bulk flow of the CF3g sample agrees remarkably well (~4° apart) with that of the bulk component of the Local Group velocity (~455 km/s in the direction $l \sim 299$, $b \sim 15$). This latter is obtained subtracting from the velocity of the LG with respect to the CMB (~631 km/s in the direction $l \sim 270$, $b \sim 27$ [72]) the local perturbations due to the infall of the LG onto the Virgo cluster (~185 km/s in the direction $l \sim 284$, $b \sim 74$ (e.g. [73,74])) as well as to the repulsion from the local void (259 km/s in the direction $l \sim 210$, $b \sim -2$) [73]). This alignment suggests that most of the LG motion is indeed generated by sources at a distance not less than the depth of the samples analyzed here, i.e. $z \sim 0.05$.

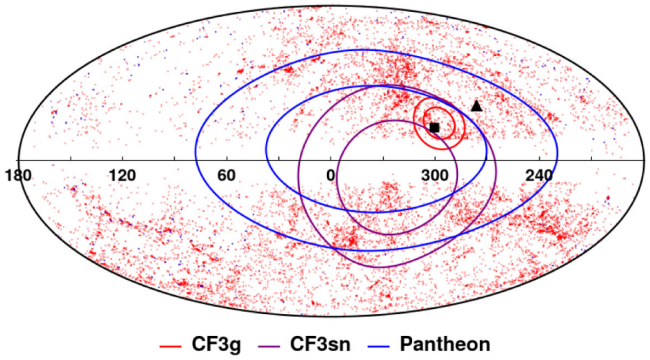

FIG. 10. Likelihood contours (1σ and 2σ) for the direction of the dipole reconstructed using 12 pixels for the CF3g (red lines), CF3sn (purple lines) and Pantheon (blue lines) samples. For reference, the direction of the motion of the barycenter of the Local Group with respect to the CMB $(l, b) \approx (270, 27)$ [72] is marked (black triangle) together with the direction of its bulk component $(l, b) \approx (299, 15)$ (black square).

We also confirm that the bulk motion traced by the CF3g sample points in the general direction in which the most massive concentrations in this region of the sky are located, namely Hydra-Centaurus (~302, $l \sim 21$) and the Shapley supercluster ($l \sim 311$, $b \sim 32$) (which are about 6 and 19 degrees away, respectively).

The amplitude of the bulk flow estimated from the CF3sn ($v_b = 195 \pm 57$ km/s) is comparable with that measured using the Pantheon sample (243 ± 110 km/s) and both values are statistically compatible with the result obtained using the CF3g sample (307 ± 23 km/s), although the large error on the latter sample makes agreement almost a foregone conclusion. These different samples also agree on the direction of the velocity field which is best determined using the total CF3 sample ($l = 285 \pm 5, 11 \pm 4$).

Comparing our results with those in the literature, we find 2σ overlap with those of [75], who, using a different compilation of redshift-independent distances covering approximately the same volume of the CF3 sample, found $v_b = 252 \pm 11$, $l = 293 \pm 5$, $b = 14 \pm 5$. They also compare favorably with those of [76] ($v_b = 292 \pm 28$ km/s, $l = 296 \pm 16$, $b = 19 \pm 6$), [77] ($v_b = 249 \pm 76$ km/s, $l = 319 \pm 18$, $b = 7 \pm 14$) and [78] (257 ± 44 km/s $l = 279$, $b = 10$). Regarding the results of [79], although there is general agreement on the bulk amplitude, the directions are misaligned by about 40 degrees.

Finally, note that in addition to the bulk component, the velocity field also exhibits a quadrupole modulation.

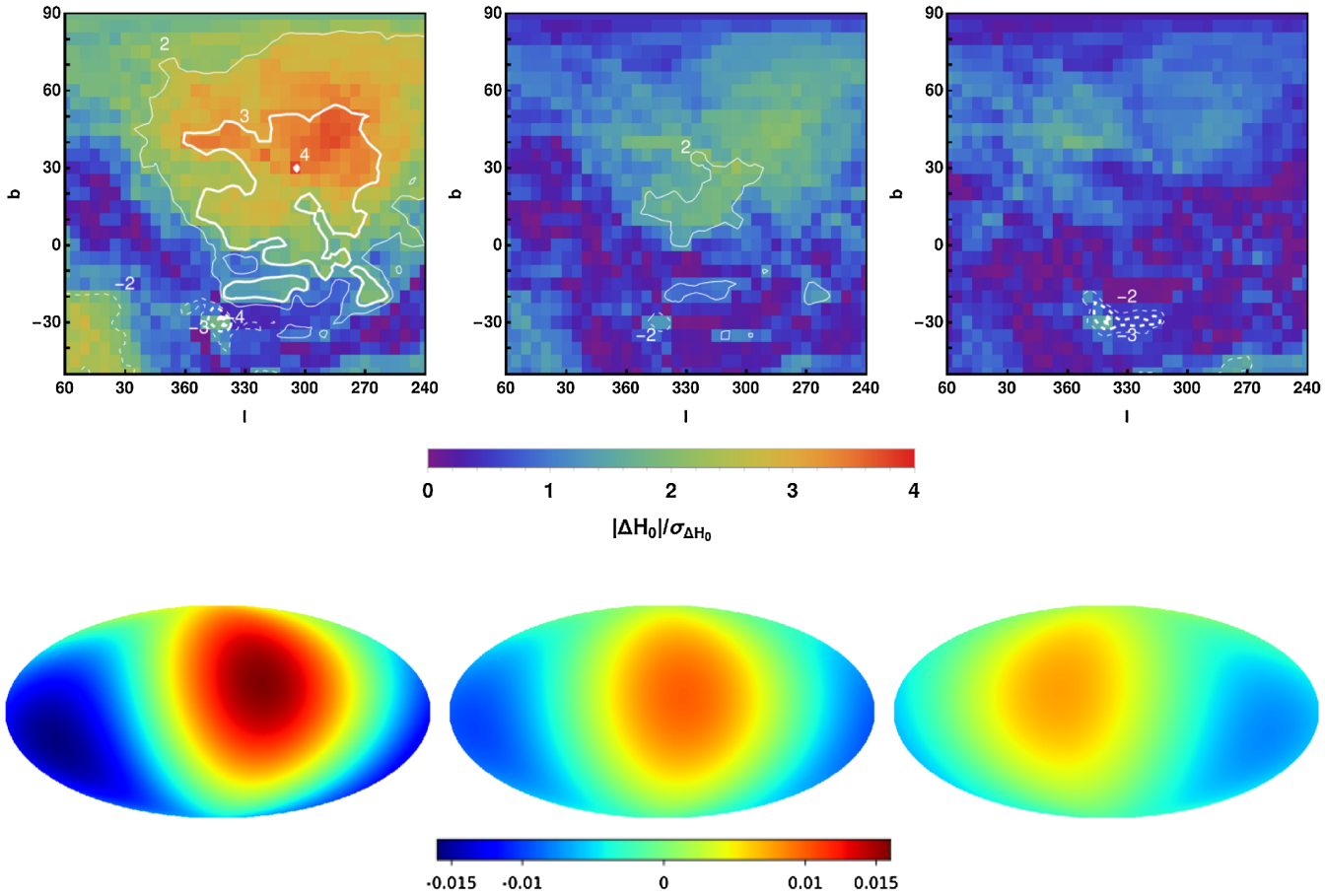

FIG. 11. Upper left panel: solid and dashed lines represent positive and negative isocontours of $\Delta H_0 = H^{\text{apex}} - H_0^{\text{antiapex}}$ calculated using Pantheon SNe with angular separation $\leq 60°$ from an axis of coordinates (l, b). Different thicknesses correspond to different amplitudes, as indicated by the labels. Isocontours are superimposed to the smoothed signal-to-noise map. Bottom left panel: the dipole component (12 pixel map) of the expansion rate fluctuation calculated using the observed redshifts. Central panels: as above, but after subtracting from the redshift of each object the peculiar velocities listed in the Pantheon catalog. Right panels: as above, but after correcting the redshift using the $\eta(\alpha)$ model (33) with Fourier coefficients computed from the CF3g data (and quoted in the fifth row of Table II). The maximum antipodal anisotropies detected are $(l, b, \Delta H_0) = (305, 30, 4.1 \pm 1.1), (305, 30, 2.4 \pm 1.1)$ and $(360, 40, 1.9 \pm 0.9)$ respectively. The best reconstructed dipolar amplitudes $(\Delta H_0 = \eta_{1(\text{max})} H_0 \ln 10)$ instead are $(334, 6, 2.6 \pm 1.0)$, $(341, 11, 1.6 \pm 1.1)$ and $(29, 7, 1.3 \pm 1.2)$ respectively.

The magnitude of this additional contribution is simply given by $v_q = a_2/a_1 v_b$. As discussed above, this component is not negligible, at least for samples CF3g and CF3sn.

C. Effects of anisotropies on the Hubble diagram

As a consequence of the alignment of the maximal intensities of its dipole, quadrupole and octupole components, the expansion field displays an "apex" towards which the rate of expansion is significantly higher than average and an antiapex where the expansions is coherently lower than the monopole component. This preferred axis characteristically shows up in the Hubble diagram.

Figure 11 shows the difference between the best estimates of H_0 deduced from the Hubble diagram analysis in two antipodal directions. In practice this is achieved by fitting the relation $\mu = 5\log(z/H_0) + 25$ separately to the distance modulus of the Pantheon objects falling in two cones of total width 120° (about 25% of the sky) centered on the observer and whose axes point in antipodal directions (apex and antiapex). Objects in sky regions where the expansion rate is larger (apex direction) do show systematically lower values of the distance modulus. The maximal deviation observed is $\Delta H_0 = 4.1 \pm 1.1$ km/s/Mpc in the direction $(l = 305, b = 30)$. For the sake of comparison, the difference is $\Delta H_0 = H_0^{\text{apex}} - H_0^{\text{antiapex}} = 5.1 \pm 0.4$ km/s/Mpc for the CF3g sample [in the direction $(l = 295, b = 5)$], $\Delta H_0 = 5.9 \pm 1.2$ km/s/Mpc for the CF3sn dataset [in the direction $(l = 280, b = -5)$] all values compatible with that obtained for Pantheon to better than 1σ.

In the standard cosmological model, anisotropies in the expansion rate are accounted for by peculiar motions.

When estimating H_0 using the Hubble diagram, it is essential to correct the observed redshifts to remove their contributions. This is done by using velocity maps derived from the linear perturbation analysis of large-scale mass fluctuations. This correction can be applied to the Pantheon catalog since, for each entry, the radial velocities (derived from the analysis of [80]) are given. Figure 11 shows the maximal antipodal anisotropy ΔH_0 after such a correction is implemented.

As it can be seen, factoring out the noncosmological contribution induced by peculiar motions reduces the amplitude of the dipolar anisotropy (now the maximal change between antipodal directions, $\Delta H_0 = 2.4 \pm 1.1$, is reduced in both amplitude and signal to noise). Although this removal is in the direction of making the results more consistent with what the standard model predicts (see, for a similar conclusion, [81]), the remaining anisotropic signal still has a nontrivial structure that makes it incompatible with being a residual fluctuation of random nature. In fact, the largest residual deviations are also the most statistically significant, as can be seen by contrasting the map of the residual signal with the signal-to-noise ratio maps (see the upper central panel of Fig. 11). The former clearly shows that, for a given distance, redshifts are systematically higher than expected over a large and contiguous region of sky.

A second remarkable fact is that the direction of the dipolar anisotropy in the Pantheon sample is not affected by removing the peculiar velocity distortions. A spherical harmonic decomposition of the expansion rate fluctuation field η (using a 12 pixel tessellation and cosmological redshifts) confirms that the angular structure of the fluctuation is preserved and only its amplitude is rescaled. Indeed, the lower central panel of Fig. 11 shows that the dipole map reconstructed after correcting the redshifts for peculiar velocities still displays an anisotropy axis pointing in the direction $(l = 341, b = 11)$. This latter is only 22 degrees away from the direction of the expansion rate reconstructed using the observed (uncorrected) redshifts ($l = 334$, $b = 6$), and still close to the direction of the bulk component of LG motion, which is in turn close to that of the CMB dipole. However, the power locked in this component is $\hat{C}_1 = 1.4 \times 10^{-4}$ nearly a factor 3 lower than what was measured by neglecting peculiar velocity effects ($\hat{C}_1 = 3.9 \times 10^{-4}$).

We checked whether this residual systematicity was the result of incorrect redshift determinations in the Pantheon catalog. In this respect, we redid the analysis using the redshift catalog made available by [82] which should also provide updates on the angular position of the host galaxies. The systematic is still detected, but this time with an even greater significance. The maximal variation of the Hubble constant between antipodal directions before applying any peculiar velocity correction is $\Delta H_0 = (4.5 \pm 1.1)$ km/s/Mpc in the direction $(l = 305, b = 30)$, After correction, both the systematic difference ($\Delta H_0 = (2.9 \pm 1.1)$ km/s/Mpc in the direction $(l = 305, b = 30)$) and the residual dipolar power ($\hat{C}_1 = 1.7 \times 10^{-4}$) are larger than in the original Pantheon catalog.

This residual signal might indicate flaws in our understanding of gravity on a local scale and might even motivate the exploration of new physics beyond the standard model. However, we will show in the following that these results rather highlight the need for further efforts to calibrate SN data if they are to be used to constrain the value of H_0 even more accurately. Mapping the observed redshift z of supernovae into the cosmological redshift z_c by subtracting from each object the peculiar velocity reconstructed at that spatial position by linear perturbation theory is indeed a far from trivial task. In addition to the uncertainties and systematics inherent to the reconstruction scheme adopted and to the samples of galaxies used to trace the matter density fluctuations, such a reconstruction is model dependent. It inevitably involves the choice of a gravitational theory and therefore the value of cosmological parameters such as, for example, the matter density parameter Ω_m.

The observable η, on the other hand, provides a neat way to take into account systematic perturbations in the expansion rate in a completely model-independent manner. We have shown that, as expected, galaxies and supernovae trace, within observational errors, the same underlying anisotropies. When estimating H_0 via the analysis of the Hubble diagram of supernovae, it is thus sufficient to remove the η fluctuations estimated from the independent galaxy catalog of redshift-independent distances. Indeed the estimated amplitude of the distance modulus is

$$\mu = 5 \log\left(\frac{z}{H_0}\right) + 25 - 5\eta, \tag{37}$$

where z is the observed redshift of the SNIa data and where η is approximated using the Legendre expansion (33) with Fourier coefficients computed from the CF3g data (and quoted in the fifth row of Table II).

The difference between the best fitting H_0 recovered in various antipodal directions by means of Eq. (37) is shown in the upper right panel of Fig. 11. The distribution of ΔH_0 values has an amplitude that is now not only reduced but also more centered on zero. Also the spherical harmonic analysis of the residual expansion rate fluctuation field $\eta(\text{pantheon}) - \eta(\text{CF3g})$ shows that the axial anisotropy is now effectively removed: the residual dipolar modulation points in the direction $(l \sim 40, b \sim 15)$ and the power locked in this component is $\hat{C}_1 = 0.8 \times 10^{-4}$, about twice as small than the residual signal obtained after correcting redshifts with the peculiar velocity field model.

The advantages of this debiasing scheme are not insignificant. First, we achieve better anisotropy subtraction with a three-parameter model [cf. Eq. (33)] than using corrected distance modules using numerical grids of

peculiar velocities. In addition, correcting for η fluctuations has a significant impact on the estimate of H_0. The Hubble parameter that best fits the Pantheon sample (in the range $0.01 < z < 0.05$) is larger by 2σ than that determined on the basis of observed redshifts alone ($\delta H_0 = 0.7$ km/s/Mpc). Also the normalized χ^2 (for 157 degrees of freedom) improves in a statistically significant way (from 1.03 to 0.96), signaling that data are better described by a linear redshift-distance relation.

D. The scale of anisotropies

How far does this anisotropic pattern extend? For galaxy samples, the determination of redshift-independent distances becomes problematic at high redshift. Only SN data give access to the deep regions of the universe. However, the SN sample is very incomplete in its coverage of the sky, a fact that prevents the extension of the study of angular anisotropies beyond the $z = 0.05$ limit.

Many studies seem to agree that the expansion rate is slightly higher in the direction of the generic CMB dipole (see [83] for a review) even at redshifts much higher than those we investigated. However, the reported magnitude of this anisotropy depends on the sample analyzed and, for the same sample, seems to depend on the technique used to measure it (e.g. [17]). The statistical significance of deviations from uniformity is also at stake. For example, with regard to studies of supernovae samples, some papers either indicate their significance, and thus the potential biasing effect on the inference of cosmological parameters [36], or refute them as pure statistical fluctuation [19,84].

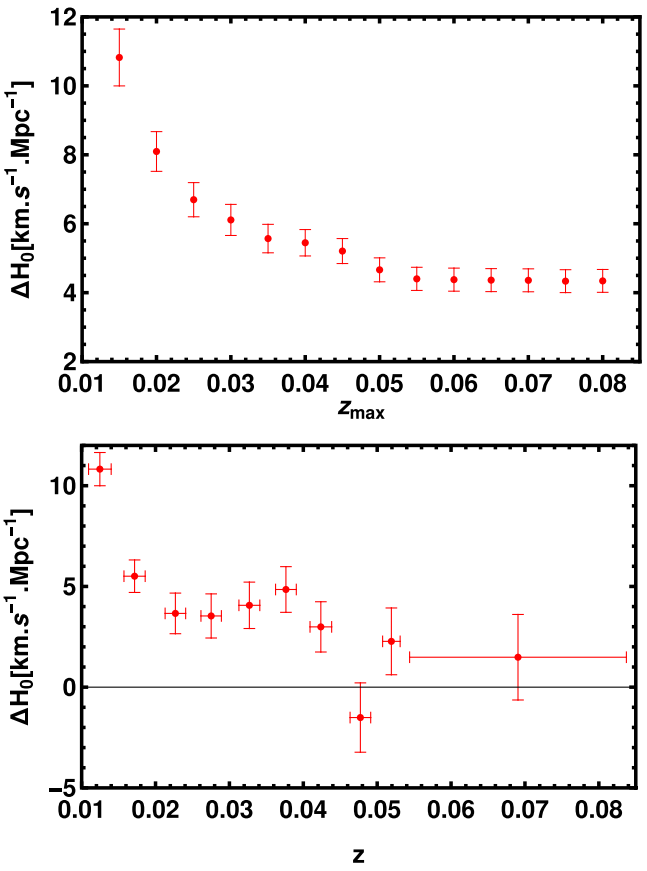

FIG. 12. Difference between the best fitting antipodal values of H_0 for CF3 objects. The Hubble diagram is constructed using objects within 60° from the apex ($l = 285, b = 11$) and antiapex directions. Points represent estimates in the cumulative intervals $0.01 < z < z_{\max}$ (upper panel) and in differential intervals (lower panel).

Figure 12 shows the difference between the best fitting H_0 in the apex and antiapex direction also including all objects in the CF3 sample (also those beyond the $z = 0.05$ cut imposed for our analysis, i.e. $N = 739$ objects in the apex direction and $N = 159$ in the antiapex direction). It is fair to say that the problem of characterizing the extent of the radial scale of the local anisotropy remains unanswered by current data.

It is clear that, from the point of view of the Standard Model, the anisotropy of the Hubble diagram should be suppressed as a function of distance if the amplitude of the peculiar motions has an upper limit. Therefore, it would be surprising if the anisotropy of the expansion rate fluctuation extended consistently beyond $z \sim 0.1$. However, as detailed above, even if the contribution of the peculiar velocities is modeled and subtracted, the structure of the residual anisotropy in the expansion rate fluctuations remains unchanged. This is a fact that should not be overlooked, as it could be an indication of possible shortcomings of the standard gravitational paradigm.

VI. CONCLUSION

The failure to converge on a consensus value of the Hubble's constant triggered investigations into the reliability of geometric descriptions of the local spacetime that deviate from the standard cosmological metric. The question that arises is whether metrics with lower symmetries, while still simple, provide a reliable description of the data in the local patch of the universe where global uniformity is violated.

We address this problem, from a new angle, trying to go beyond the standard perturbative approaches by which nonuniformities in the local expansion rate are accounted for in the standard model. To this end, we have designed an observable that captures, in a statistically unbiased way, the average angular fluctuations in the local expansion rate. The observable η is fully model independent not requiring any knowledge about the metric, the gravity model or the amount of matter in the Universe. On the contrary, it is sensitive, and therefore instrumental to understand local violations of the cosmological principle, i.e. how far the spatial distribution of matter is from being homogeneous and how far the kinematics of the cosmic expansion is from being isotropic. In the limit of small fluctuations, a perturbative expansion around the FRW expectation shows

that $\eta \propto \delta H_0/H_0$, i.e. it measures the relative fluctuations in the Hubble parameter. For this reason, the monopole of the expansion rate field vanishes and the η observable is practically insensitive to the actual value of H_0.

We have estimated the η field using catalogs of redshift-independent distances such as the Cosmicflows-3 galaxy sample and the Pantheon sample of supernovae. We have then compressed the resulting signal into independent spherical harmonics components to better analyze the structure of the anisotropies in the linear redshift-distance relation. Particular care was paid to assess the reliability of the reconstructions, either analytically, computing the variance of relevant SH parameters, or numerically by means of Monte Carlo simulations. This last approach has the advantage of also correcting the systematic bias induced by the scarcity and incompleteness of the data used in our analysis as well as by the pixelization strategies applied to them.

All data samples analyzed consistently suggest the existence of a preferred axis in the local universe ($0.01 < z < 0.05$), in the direction $(l, b) = (285 \pm 5, 11 \pm 4)$, along which the local redshift-distance relation displays a dipolar pattern. Within the standard model of cosmology, notably its linear perturbative extension, this dipolar modulation of the angular expansion rate can be understood as the imprint of a large-scale bulk flow model. We find that galaxies inside the survey volume $r < 150h^{-1}$ Mpc coherently moves with an average speed $v_b = (299 \pm 22)$ km/s. This direction agrees fairly well with the estimated direction of the bulk component of the Local Group velocity $(l, b) \approx (299, 15)$ [73] and confirms that the LG participates in a bulk flow that extends out to distances of at least $z = 0.05$.

Interestingly, the SH analysis suggests that a simple dipole provides a poor representation of the angular fluctuations in the local expansion rate. A more sophisticated description is necessary if we are to properly model the anisotropies in the redshift-distance relation. We find that about 50% of the anisotropic signal is contributed by a quadrupole component. This is independently confirmed by the CF3g and CF3sn samples, which also consistently show that the axis of maximal expansion of the quadrupole is aligned with the direction of the dipole. This intriguing feature persists when the sample is split in two and the analysis is repeated in two separate spherical shells of different depths. This evidence allows us to exclude the possibility that the observed alignment is a casual coincidence, that is, a volume-dependent fluke. The analyses of both samples also agree on the shape of the quadrupole. It is a rather axisymmetrical configuration, with no indication of prominent secondary axes.

The findings about the alignment of the quadrupole in the general direction of the dipole independently confirms results of [50] or, more recently, of [38] who, using smaller samples, showed that the eigenvector expansion of the shear tensor (a proxy for the quadrupole moment) is aligned in the direction of the Hydra-Centaurus/Shapley superclusters. We extend the validity of these results over a volume 4 times larger through a separate analysis of the galaxy and SN samples. Furthermore, we find that the octupole is also involved in the alignment. Despite the large errors induced by the sparsity of the sample and the relatively large coarse graining of the multipole reconstruction scheme, there is indeed tentative evidence for the detection of an octupole signal, at least for the CF3 sample of galaxies. Its intensity is of similar amplitude to that of the quadrupole. Its configuration is also quite peculiar, with its axis of maximal intensity collinear with the axes of the dipole and the quadrupole.

We note, as a curiosity, that the direction where the quadrupole of the expansion field has a maximum does not coincide with that where the quadrupole of the CMB temperature fluctuations reaches its maximum. Also their configuration is different: planar for the CMB and axisymmetric for the local expansion field.

There are several independent indications confirming the robustness of our findings about the geometry of the multipolar structure of the expansion rate fluctuation field: (a) the anisotropies detected in different samples agree both in amplitude and direction, (b) the probability that they are random fluctuations is ruled out by Monte Carlo analyses, and (c) the random alignment of the independent dipole, quadrupole and, tentatively, octupole moments is statistically improbable. Given that the amplitude of the dipole, quadrupole and octupole components of the fluctuation field scale differently with distance from the gravitational sources (R, R^3 and R^5, respectively), one would expect that their peculiar configuration is due either to an extraordinary fine-tuning in the alignment of the sources themselves or to the dominant role of a single structure dominating the gravitational dynamics in the local universe. We note that indeed [85] finds evidence that the LG lies approximately on the line joining the barycenter of three large cosmic structures, the Shapley concentration and the Great Attractor on one side, and a large galactic underdensity in the diametrically opposite direction. We do not dwell on this and other possible explanations in this article, but will address this in a further study.

According to the standard model, the departures from uniformity are the manifestation of deviations from comobility induced by local gravitational fields. After factoring out from the Pantheon sample the contribution of these peculiar velocities (reconstructed by applying prescriptions of the theory of linear perturbations to the observed fluctuations in the spatial distribution of galaxies), we observe that the H_0 perturbations, although reduced in amplitude, do not distribute as random (Gaussian) residuals. Curiously, the structure of the expansion rate field still presents an axial anisotropy in the same general direction as the CMB dipole. We find that the power in the residual dipole component, as quantified by the coefficient $\hat{C}_1$, is

reduced only by about 50%, and that, as a consequence, the Hubble parameter still has a sinusoidal modulation of amplitude $\Delta H_0 = 1.6 \pm 1.1$ km/s/Mpc between the apex and antiapex directions (as opposed to $\Delta H_0 = 2.6 \pm 1.0$ before any peculiar velocity corrections).

This residual systematicity does not indicate the failure of the standard model, but rather the need to improve methods of reconstructing peculiar velocities. In this regard we show how to exploit the expansion rate fluctuation field η to subtract redshift anisotropies in a fully model-independent way. In practice, we correct the distance moduli of the Pantheon sample with a neat three-parameter Legendre expansion formula [see Eq. (33)] calibrated (and not fitted) using information extracted from the analysis of the CF3g galaxy sample. Despite its simplicity, the approach proves effective: not only is the dipole pattern suppressed by a factor of about 5 in power, but even its direction is now offset from the general direction of the CMB dipole. The low signal-to-noise ratio of the residuals is also consistent with the virtual absence of any systematicity. As a result, the best-fit Hubble parameter is 0.7 km/s/Mpc higher than if the distance modulus were calculated with the observed redshifts, and also the goodness of fit, as measured by the χ^2_ν, improves in a statistically significant way.

In addition to the similarities among results inferred from independent samples, there are also differences that require further study. Of these, the most intriguing is the fact that no quadrupole nor octupole component shows up in the Pantheon catalog. This is essentially due to the fact that this catalog contains virtually no objects in the direction where the $l = 1, 2, 3$ multipole aligns. This also explains why the axisymmetric η model calibrated using the CF3g and CF3sn datasets, and which incorporates quadrupolar and octupolar contributions, also effectively explains the purely dipolar anisotropies characteristic of the Pantheon data sample. It would therefore be very useful to look for SN candidates in this critical region of the sky if one wants to advance towards a more solid understanding of the anisotropies in the local expansion rate.

To conclude, a key objective has been to show, as a proof of concept, the potential power of a new observable, the expansion rate fluctuation η, both to study the structure of the anisotropies in the redshift-distance relation and to minimize eventual systematics in the locally inferred value of H_0. It is thus necessary, in follow-up papers, to build on the current formalism by doing a more intensive data analysis. This will include the use of updated and expanded datasets, including Cosmicflows-4 [86], Pantheon+ [87]. It will also involve parallel analysis of large suites of N-body simulations of local patches of the universe to assess the typicality of the results we have found by taking into account the cosmic variance. It will be also interesting to explore the theoretical consequences of our analysis and interpret the salient features of the local expansion field in terms of alternative metrics (e.g. [88,89]) with the goal of extending the predictive power of the FRW model to subuniform cosmic scales.

ACKNOWLEDGMENTS

We would like to thank Pierre Fleury, J. Larena, Roy Maartens, Federico Piazza, and Licia Verde for useful discussions. We also thank the M2 student Pierre Ciccodicola who participated in the initial phase of this work. This study was partially supported by the *Institut Physique de l'Univers* (IPHU Grant No. 013/2020) and by the Programme National GRAM of Centre National de la Recherche Scientifique/Institut National des Sciences de l'Univers with Institut National de Physique and Institut National de Physique Nucléaire et de Physique des Particules cofunded by Centre National d'Etudes Spatiales.

APPENDIX A: DEALING WITH HEALPIX MATRICES

We estimate the SH coefficients $a_{\ell m}$ by passing the HEALPIX iteration scheme and exploiting, instead, the closed-form expression given by Eq. (23). To compute it in practice, it is necessary to compress the SH $a_{\ell m}$ coefficients into a 1D matrix, that is, to suppress a labeling index. There are many ways to do this; we do it so that the row vector $\boldsymbol{a}$ contains as elements

$$\boldsymbol{a}^T = \{a_{00}, a_{10}, a_{20}, \ldots, a_{\ell_{\max}0}, a_{11}, a_{21}, \ldots, a_{\ell_{\max}1}, \ldots, a_{\ell_{\max}\ell_{\max}}, a_{1-1}, a_{2-1}, \ldots, a_{\ell_{\max}-1}, \ldots, a_{\ell_{\max}-\ell_{\max}}\}.$$

If we identify with the index j (starts from 1) each vector component, the relations between j and l and m are

$$m_j = \begin{cases} -\left[\!\left[\sqrt{(\ell_{\max}+\frac{1}{2})^2 + 2(\ell_{\max}+1-j)} - \frac{1}{2} - \ell_{\max}\right]\!\right], & j \le \nu \\ \left[\!\left[\sqrt{(\ell_{\max}+\frac{1}{2})^2 - 2(j-\nu)} - \frac{1}{2} - \ell_{\max}\right]\!\right], & j > \nu, \end{cases}$$

where ν is the number of $a_{\ell m}$ with $m \ge 0$ until $\ell_{\max}$, so $\nu = \frac{1}{2}(\ell_{\max}+1)(\ell_{\max}+2)$, and $[\![]\!]$ is the floor function.

$$\ell_j = j - \mathcal{N}_{m_j} + \ell_{\max}$$

and

$$j = \mathcal{N}_m + \ell - \ell_{\max},$$

where $\mathcal{N}_m$ is

$$\mathcal{N}_m = \begin{cases} m(\ell_{\max}+\frac{1}{2}) + \ell_{\max} + 1 - \frac{m^2}{2}, & m \geq 0 \\ (\ell_{\max}-m)(\ell_{\max}+\frac{1}{2}) + \ell_{\max} + 1 - \frac{1}{2}(\ell_{\max}^2 + m^2), & m < 0. \end{cases}$$

The elements of the matrix $\boldsymbol{A}$ [cf. Eq. (16)] are thus

$$A_{jp} = \frac{4\pi}{N_{\rm pix}} Y^*_{\ell_j,m_j}(\theta_p, \phi_p)$$

and its dimension is given by $(\ell_{\max}+1)^2 \times N_{\rm pix}$. It follows that

$$\hat{a}^{(0)}_{\ell_j m_j} = \sum_{p=1}^{N_{\rm pix}} A_{jp}\eta(p).$$

Since $\boldsymbol{S} = \frac{N_{\rm pix}}{4\pi}\boldsymbol{A}^{*T}$, and $\boldsymbol{M} = (\boldsymbol{AB})^{-1}$, we can thus write Eq. (23) explicitly as

$$\hat{a}_{\ell_i m_i} = \sum_{j=1}^{(\ell_{\max}+1)^2} M_{ij} a^{(0)}_{\ell_j m_j},$$

where $\hat{a}_{\ell m}$ are the elements of the vector $\boldsymbol{a}^{(\infty)}$.

APPENDIX B: VARIANCE OF THE ESTIMATOR $\hat{a}_{\ell m}$

The statistical errors affecting the estimates of the SH coefficients can be estimated analytically. We start by noticing that the zeroth order value of the SH coefficients is given by Eq. (13). The variances of its real and imaginary parts are

$$V[\Re[\hat{a}^{(0)}_{\ell m}]] = \left(\frac{4\pi}{N_{\rm pix}}\right)^2 \sum_{p=1}^{N_{\rm pix}} \sigma^2(p)(Y^*_{\ell m}(\theta_p, 0)\cos(m\phi_p))^2$$

$$V[\Im[\hat{a}^{(0)}_{\ell m}]] = \left(\frac{4\pi}{N_{\rm pix}}\right)^2 \sum_{p=1}^{N_{\rm pix}} \sigma^2(p)(Y^*_{\ell m}(\theta_p, 0)\sin(m\phi_p))^2,$$

where

$$\sigma^2(p) = \frac{1}{\sum_{i=1}^{N_{g(\text{in pixel p})}} \frac{1}{\delta_i^2}}$$

is the variance affecting the estimate of $\eta(p)$, the expansion rate fluctuation in pixel p. Note that complex conjugation is not anymore effective since $Y_{\ell m}(\theta_p, 0)$ is real. Since also η is a real field, then $a_{l-m} = (-1)^m a^*_{\ell m}$, which implies that the SH coefficients are not independent random variables. To overcome this issue we express $a^{(\infty)}_{\ell m}$ as a linear combination of $a^{(0)}_{\ell m}$, with $m \geq 0$. To this end we need to decompose $\boldsymbol{M}$ [see Eq. (23)] into its real ($\boldsymbol{\mathcal{R}}$), and imaginary ($\boldsymbol{\mathcal{I}}$) parts, so that

$$\begin{aligned}\Re[a^{(\infty)}_{\ell_i m_i}] = &\sum_{j=1}^{\ell_{\max}+1} \mathcal{R}_{ij}\Re[a^{(0)}_{\ell_j 0}] \\ &+ \sum_{j=\ell_{\max}+2}^{\nu} [(\mathcal{R}_{ij} + (-1)^{m_j}\mathcal{R}_{i(j+\nu-\ell_{\max}-1)})\Re[a^{(0)}_{\ell_j m_j}] \\ &- (\mathcal{I}_{ij} + (-1)^{m_j+1}\mathcal{I}_{i(j+\nu-\ell_{\max}-1)})\Im[a^{(0)}_{\ell_j m_j}]]\end{aligned}$$

and

$$\begin{aligned}\Im[a^{(\infty)}_{\ell_i m_i}] = &\sum_{j=1}^{\ell_{\max}+1} \mathcal{I}_{ij}\Re[a^{(0)}_{\ell_j 0}] \\ &+ \sum_{j=\ell_{\max}+2}^{\nu} [(\mathcal{R}_{ij} + (-1)^{m_j+1}\mathcal{R}_{i(j+\nu-\ell_{\max}-1)})\Im[a^{(0)}_{\ell_j m_j}] \\ &+ (\mathcal{I}_{ij} + (-1)^{m_j}\mathcal{I}_{i(j+\nu-\ell_{\max}-1)})\Re[a^{(0)}_{\ell_j m_j}]].\end{aligned}$$

We thus obtain

$$\begin{aligned}V[\Re[\hat{a}_{\ell_i m_i}]] = &\sum_{j=1}^{\ell_{\max}+1} \mathcal{R}_{ij}^2 V[\Re[a^{(0)}_{\ell_j 0}]] \\ &+ \sum_{j=\ell_{\max}+2}^{\nu} [(\mathcal{R}_{ij} + (-1)^{m_j}\mathcal{R}_{i(j+\nu-\ell_{\max}-1)})^2 V[\Re[a^{(0)}_{\ell_j m_j}]] \\ &+ (\mathcal{I}_{ij} + (-1)^{m_j+1}\mathcal{I}_{i(j+\nu-\ell_{\max}-1)})^2 V[\Im[a^{(0)}_{\ell_j m_j}]]]\end{aligned}$$

and

$$\begin{aligned}V[\Im[\hat{a}_{\ell_i m_i}]] = &\sum_{j=1}^{\ell_{\max}+1} \mathcal{I}_{ij}^2 V[\Re[a^{(0)}_{\ell_j 0}]] \\ &+ \sum_{j=\ell_{\max}+2}^{\nu} [(\mathcal{R}_{ij} + (-1)^{m_j+1}\mathcal{R}_{i(j+\nu-\ell_{\max}-1)})^2 V[\Im[a^{(0)}_{\ell_j m_j}]] \\ &+ (\mathcal{I}_{ij} + (-1)^{m_j}\mathcal{I}_{i(j+\nu-\ell_{\max}-1)})^2 V[\Re[a^{(0)}_{\ell_j m_j}]]]\end{aligned}$$

and, in the end, the variance

$$\sigma^2_{\ell m} \equiv V[\hat{a}_{\ell m}] = V[\Re[\hat{a}_{\ell m}]] + V[\Im[\hat{a}_{\ell m}]]. \quad \text{(B1)}$$

APPENDIX C: MONTE CARLO ESTIMATION OF MEASUREMENT ERRORS

We determine the errors, both statistical and systematic, that plague the SH reconstruction by means of Monte Carlo simulations. We consider as input model the Fourier coefficients (up to $\ell_{\max}$) measured from the data, and we use them to simulate a fiducial η field. We then randomly perturb the expansion field, at the angular position of the objects, by means of a Gaussian noise with mean value η and with standard deviation δ. We construct in this way a suite of 1000 mock catalogs which are tessellated with HEALPIX and Fourier transformed in

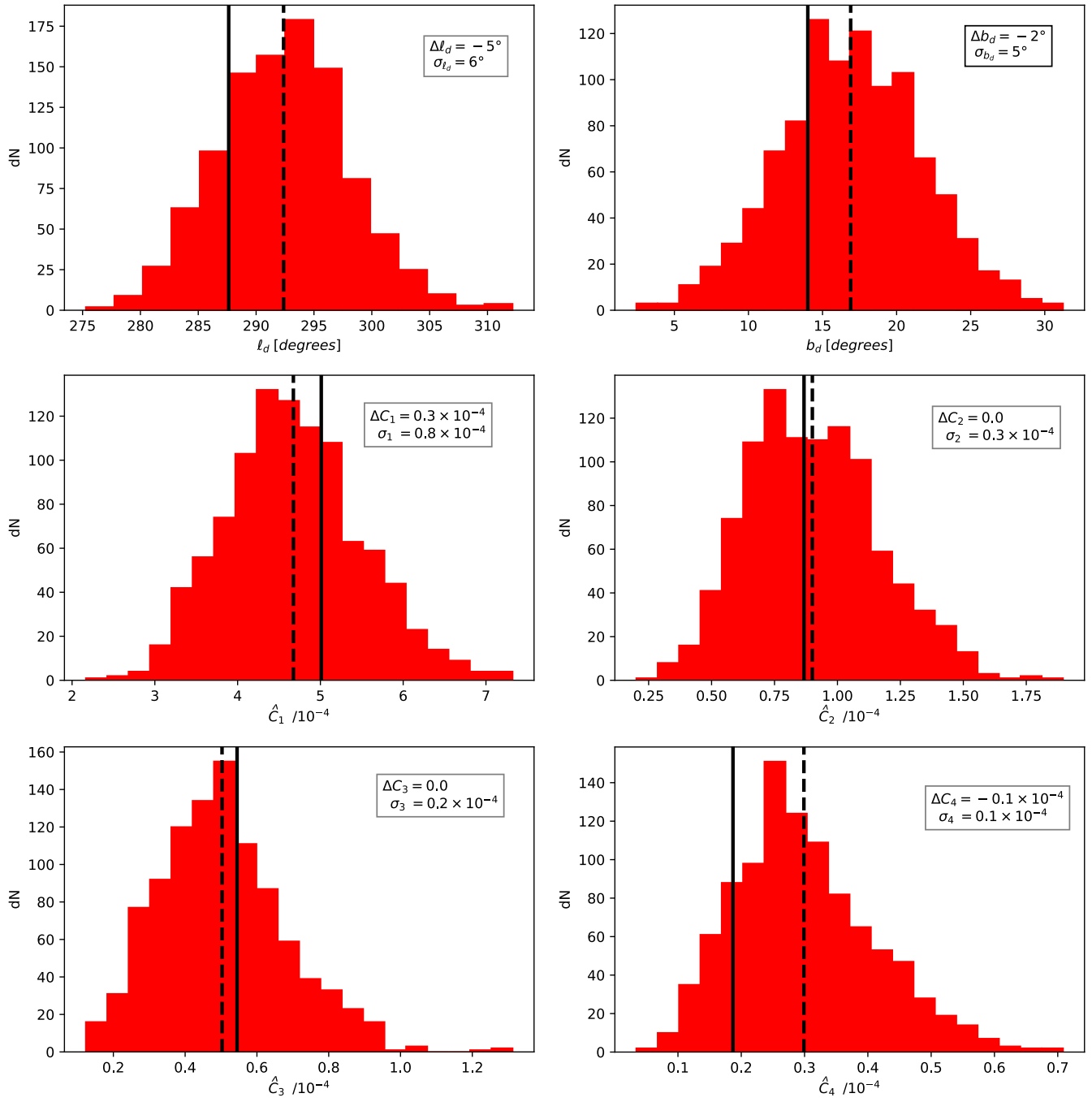

FIG. 13. Distribution of relevant SH parameters recovered from analyzing, with the same pipeline used for real data, 1000 Monte Carlo simulations of the CF3 galaxy sample [0.01, 0.05] (48 pixels). The parameters of interest are the power spectrum coefficients $\hat{C}_\ell$ and the direction of the dipole (in galactic coordinates). The black line displays the simulated input value (fiducial model), while the dashed black line corresponds to the average of the distribution.

exactly the same way as the data. This means we apply the same rotation scheme to fill all the pixels with objects, and the same numerical scheme to calculate the power spectrum (up to $\ell_{\max}$). The resulting distribution of the output signals, notably the sky coordinates where the dipole and quadrupole signals are maximal and the amplitude of the power spectrum coefficient $\hat{C}_\ell$ is finally reconstructed and analyzed to assess the confidence level with which our analysis pipeline retrieves the fiducial input values.

Results for the CF3 and CF3sn samples are shown in Figs. 13 and 14 respectively, and quantitatively summarized in Tables IV and III. Both Figs. 13 and 14 show that the systematic errors that affect our analysis, defined as the difference between the input parameter and the average value inferred by means of the Monte Carlo simulations, are always smaller than the statistical error. However, they are non-negligible and we thus correct the observational measurements presented in Table I for these bias factors.

In Table III we compare the standard deviation of the $\hat{C}_\ell$ coefficients estimated by Monte Carlo simulations with that obtained by applying Eq. (29). There is an excellent agreement between the numerical and analytical estimates. The small remaining discrepancy can be mainly attributed to two effects. First, the estimator $\hat{a}_{\ell m}$ is a biased estimator for $a_{\ell m}$ and that is not included in Eq. (29). Also the finite number of Monte Carlo realizations (1000) contributes to the small discrepancies we observe.

An alternative strategy to test the reliability of the reconstruction consists in determining the value of the coefficients $a_{\ell m}$ not via a deterministic scheme [cf. Eq. (23)] but by means of a maximum likelihood analysis. We thus look for the set of SH parameters that minimize the quantity

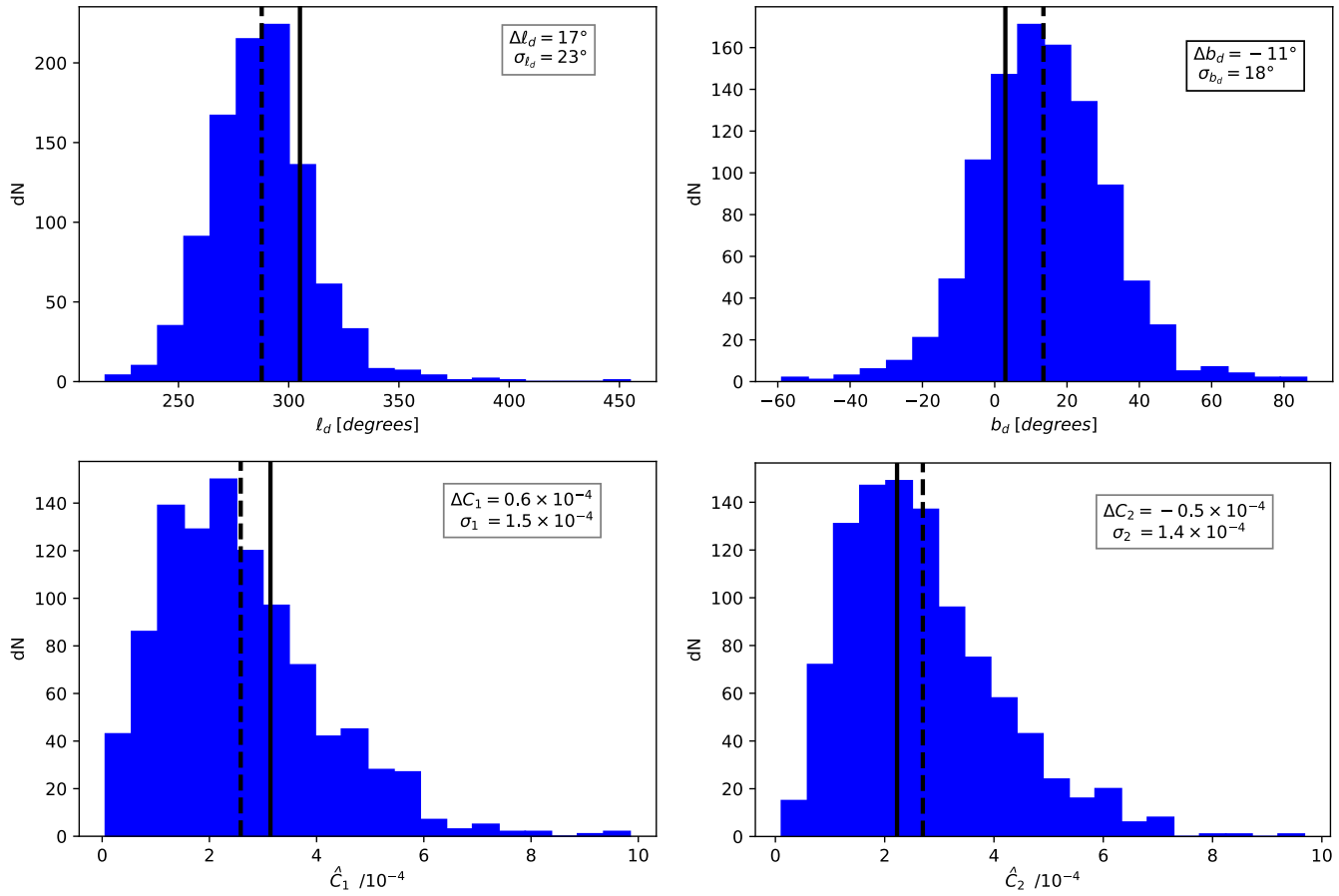

FIG. 14. Same as in Fig. 13, but for the CF3sn sample [0.01, 0.05] (12 pixels).

TABLE III. The standard deviation of the $\hat{C}_\ell$ coefficients reconstructed using the various samples displayed in the first column. For each sample, and for each $\hat{C}_\ell$, we compare error estimates obtained numerically (by means of 1000 Monte Carlo simulations) and analytically [by means of Eq. (29)].

		$\sigma_{\hat{C}_1}$ (10^{-4})		$\sigma_{\hat{C}_2}$ (10^{-4})		$\sigma_{\hat{C}_3}$ (10^{-4})	
Sample	$N_{\rm pix}$	Numerical	Analytical	Numerical	Analytical	Numerical	Analytical
CF3 [0.01, 0.05]	192	1.6	1.6	0.9	1.0	0.4	0.4
CF3 [0.01, 0.05]	48	0.8	0.9	0.3	0.3	0.2	0.2
CF3g [0.01, 0.05]	48	1.0	1.2	0.4	0.4	0.2	0.3
CF3 [0.01, 0.05]	12	0.8	0.8	0.3	0.3	⋯	⋯
CF3g [0.01, 0.05]	12	0.6	0.7	0.4	0.4	⋯	⋯
CF3sn [0.01, 0.05]	12	1.5	1.9	1.5	1.4	⋯	⋯
Pantheon [0.01, 0.05]	12	2.7	3.1	1.4	1.7	⋯	⋯
CF3 [0.01, 0.03]	12	1.0	1.2	0.6	0.7	⋯	⋯
CF3 [0.03, 0.05]	12	0.7	0.7	0.3	0.4	⋯	⋯

TABLE IV. The systematic bias factor for different parameters of the SH reconstruction. The systematic error is computed using 1000 Monte Carlo simulations of the catalogs displayed in the first column.

Sample	$N_{\rm pix}$	Δl_d	Δb_d	ΔC_1 (10^{-4})	Δl_q	Δb_q	ΔC_2 (10^{-4})	Δl_t	Δb_t	ΔC_3 (10^{-4})
CF3 [0.01, 0.05]	192	0	−2	−0.5	1	0	−0.1	5	−2	−0.4
CF3 [0.01, 0.05]	48	−5	−2	0.3	−1	−4	0	−2	−3	0
CF3g [0.01, 0.05]	48	0	−2	1.3	5	1	−0.1	−16	−2	0
CF3 [0.01, 0.05]	12	−1	−4	0	−5	3	0.1	⋯	⋯	⋯
CF3g [0.01, 0.05]	12	0	−4	0	12	7	0	⋯	⋯	⋯
CF3sn [0.01, 0.05]	12	17	−11	0.6	11	5	−0.5	⋯	⋯	⋯
Pantheon [0.01, 0.05]	12	13	−14	−1.1	⋯	⋯	−1.0	⋯	⋯	⋯
CF3 [0.01, 0.03]	12	0	−5	0.7	1	−3	0.5	⋯	⋯	⋯
CF3 [0.03, 0.05]	12	1	1	−0.3	2	7	0.1	⋯	⋯	⋯

TABLE V. Best fitting SH parameters obtained by minimizing the χ^2 difference between the expansion field $\hat{\eta}(\mathbf{r})$ and a model given by cutting the SH decomposition at $\ell = 2$. A total of eight $a_{\ell m}$ parameters are fitted to the data.

Sample	l_d	b_d	$\hat{C}_1$ (10^{-4})	$\hat{C}_2$ (10^{-4})	$\frac{\chi^2_{\min}}{\mathrm{dof}}$
CF3 [0.01, 0.05]	287 ± 5	10 ± 4	4.3 ± 0.8	1.2 ± 0.3	1.26
CF3g [0.01, 0.05]	290 ± 5	5 ± 4	5.3 ± 0.9	1.3 ± 0.3	1.25
CF3sn [0.01, 0.05]	293 ± 14	0 ± 10	5.5 ± 2.6	1.8 ± 1.1	1.60
Pantheon [0.01, 0.05]	311 ± 32	35 ± 36	3.4 ± 2.1	0.5 ± 0.9	0.98
CF3 [0.01, 0.03]	280 ± 5	11 ± 4	8.0 ± 1.4	2.4 ± 0.5	1.37
CF3 [0.03, 0.05]	324 ± 17	10 ± 12	1.4 ± 0.8	1.4 ± 0.5	1.16
CF3sn [0.01, 0.03]	274 ± 14	-5 ± 11	8.2 ± 4.3	3.1 ± 1.9	1.81
CF3sn [0.03, 0.05]	325 ± 23	6 ± 18	5.9 ± 5.0	0.9 ± 1.1	1.24

$$\chi^2 = \sum_{i=1}^{N} \left(\frac{\hat{\eta}(\mathbf{r}_i) - \eta(\theta_i, \phi_i)}{\delta_i^2} \right)^2, \tag{C1}$$

where N is, depending on the catalog, either the number of galaxies or SNIa. The theoretical model that describes the expansion rate fluctuations is

$$\eta(\theta,\phi) = \sum_{\ell=\ell_{\min}}^{\ell_{\max}} \sum_{m=-\ell}^{\ell} a_{\ell m} Y_{\ell m}(\theta,\phi) = \sum_{\ell=\ell_{\min}}^{\ell_{\max}} \Big[a_{\ell 0} Y_{\ell 0}(\theta,\phi) + 2 \sum_{m=1}^{m=\ell} (\Re[a_{\ell m}] Y_{\ell m}(\theta,0) \cos(m\phi) - \Im[a_{\ell m}] Y_{\ell m}(\theta,0) \sin(m\phi)) \Big], \tag{C2}$$

TABLE VI. Best fitting SH parameters obtained by minimizing the χ^2 difference between the expansion field $\hat{\eta}(\mathbf{r})$ and a model given by cutting the SH decomposition at $\ell = 3$. A total of 15 independent parameters are fitted to the data.

Sample	l_d	b_d	$\hat{C}_1$ (10^{-4})	$\hat{C}_2$ (10^{-4})	$\hat{C}_3$ (10^{-4})	$\frac{\chi^2_{\min}}{\mathrm{dof}}$
CF3 [0.01, 0.05]	282 ± 5	13 ± 4	5.0 ± 0.9	1.0 ± 0.2	0.6 ± 0.2	1.26
CF3g [0.01, 0.05]	285 ± 5	8 ± 4	6.0 ± 1.2	1.1 ± 0.3	0.7 ± 0.2	1.25
CF3sn [0.01, 0.05]	285 ± 16	2 ± 11	5.6 ± 3.1	2.4 ± 1.4	1.5 ± 1.1	1.60
Pantheon [0.01, 0.05]	247 ± 34	20 ± 23	7.3 ± 8.4	2.0 ± 3.2	2.4 ± 2.3	1.01
CF3 [0.01, 0.03]	279 ± 6	15 ± 5	7.3 ± 1.5	2.2 ± 0.4	1.1 ± 0.3	1.36
CF3 [0.03, 0.05]	323 ± 21	14 ± 14	1.5 ± 1.0	1.6 ± 0.7	0.2 ± 0.2	1.16

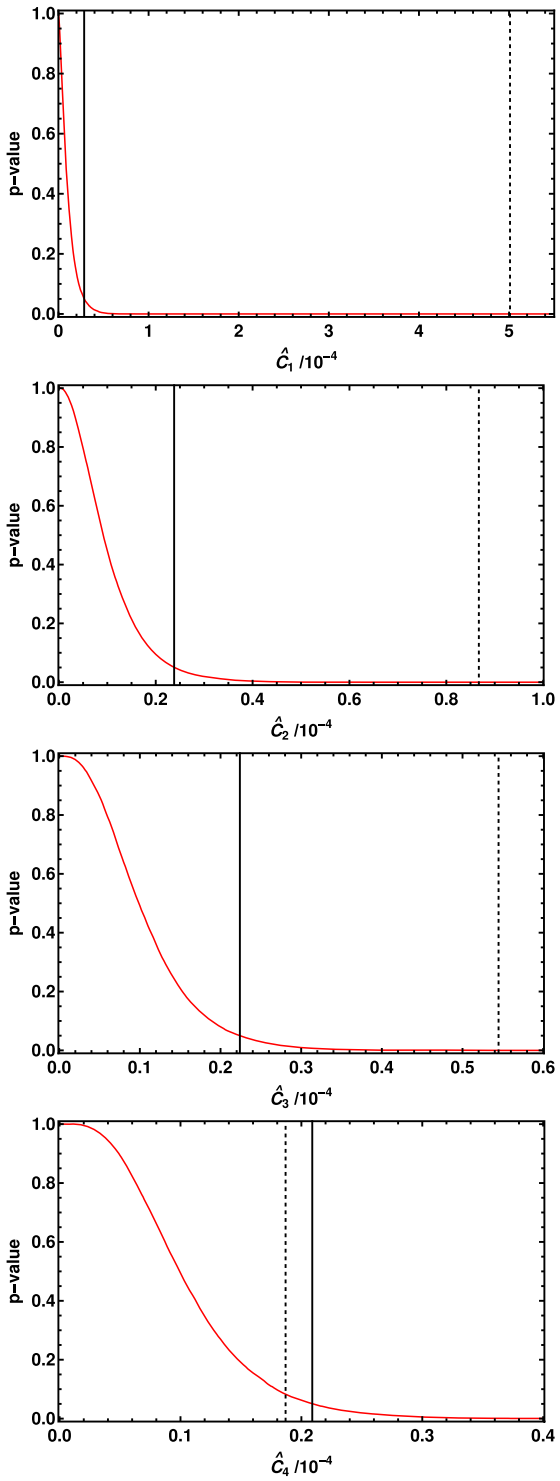

FIG. 15. Probability (p-values) of obtaining a power spectrum coefficient larger than $\hat{C}_\ell/10^{-4}$, when the underlying model does not have any multipole. The black dashed line displays the value of $\hat{C}_\ell$ actually measured in the CF3 sample, partitioned into 48 pixels. Estimates are based on 10000 Monte Carlo simulations of the CF3 sample. The p-values for the $\hat{C}_\ell$ actually measured are 0%, 0%, 0.01%, 8.27% respectively for the first four $\hat{C}_\ell$. The black solid line indicates the value of $\hat{C}_\ell$ which has the threshold p-value for acceptance (5%).

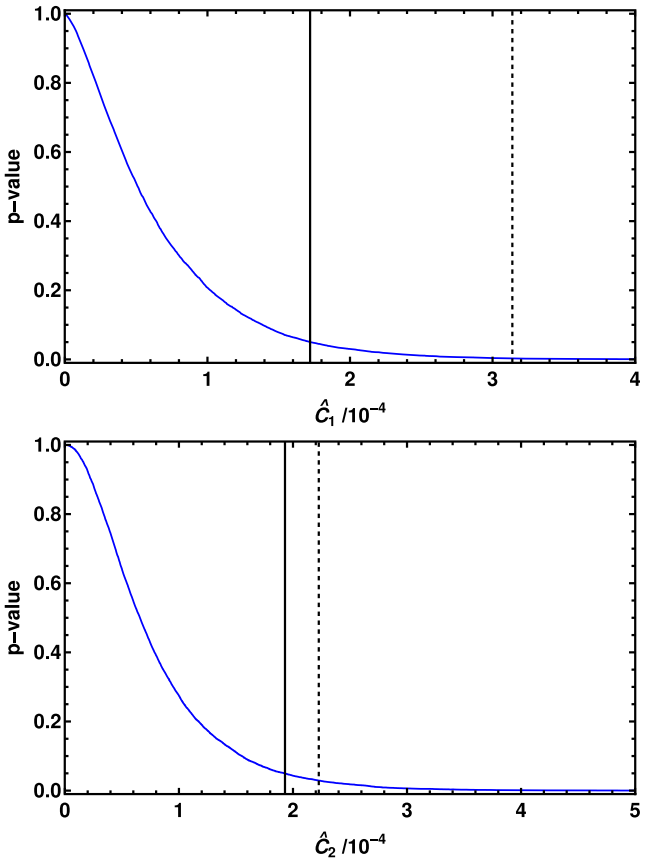

FIG. 16. Same as in Fig. 15 but using simulations of the CF3sn sample tessellated into 12 pixels.

where $\ell_{\rm min}$ and $\ell_{\rm max}$ are the lowest and maximum multipole fitted. The above expression accounts for the fact that $a_{\ell-m}$ and $a_{\ell m}$ are not independent coefficients since η is a real field and we only have to choose one of them as a free parameter in the fit. The χ^2 statistic is then minimized with respect to the real and imaginary part of $a_{\ell m}$ (with $m \geq 0$).

We choose $\ell_{\rm min} = 1$ and run two independent analyses using $\ell_{\rm max} = 2$ and $\ell_{\rm max} = 3$ respectively. The resulting best fitting parameters together with the associated errors, are reported in Tables V and VI.

The estimates deduced by means of this statistical approach are in excellent agreement with the Fourier determinations (cf. Table I). This provides independent supporting evidence of the robustness of the results obtained in Sec. V. Also the minimum value of the normalized χ^2 statistic is of relevance.

Finally, we also quantify the probability that the measured multipolar signals are statistical flukes due to the sparsity and angular anisotropy of the analyzed samples. To this end we compute, using 10000 Monte Carlo simulations, the probability (p-values) of measuring a power spectrum coefficient greater than a given nonzero value when the underlying input model does not have any multipole. Results for the CF3, CF3sn samples are shown

in Figs. 15 and 16 respectively (see Table I for the other samples).

Comparing these results with the values of the power spectrum coefficients $\hat{C}_\ell$ inferred from the CF3g data, we see that the chance of an accidental signal is negligible for $\ell \leq 3$. Similarly, the risk of misinterpreting the CF3sn sample results is insignificant for $\ell \leq 2$.

[1] P. J. E. Peebles, *The Large-Scale Structure of the Universe* (Princeton University Press, Princeton, NJ, 1980).
[2] C. Clarkson and R. Maartens, Classical Quantum Gravity **27**, 124008 (2010).
[3] C. L. Bennett, D. Larson, J. L. Weiland, N. Jarosik, G. Hinshaw, N. Odegard, K. M. Smith, R. S. Hill, B. Gold, M. Halpern *et al.*, Astrophys. J. Suppl. Ser. **208**, 20 (2013).
[4] P. A. R. Ade *et al.* (Planck Collaboration), Astron. Astrophys. **594**, A16 (2016).
[5] P. Sarkar, J. Yadav, B. Pandey, and S. Bharadwaj, Mon. Not. R. Astron. Soc. **399**, L128 (2009).
[6] C. Marinoni, J. Bel, and A. Buzzi, J. Cosmol. Astropart. Phys. 10 (2012) 036.
[7] S. Appleby and A. Shafieloo, J. Cosmol. Astropart. Phys. 10 (2014) 070.
[8] C. A. P. Bengaly, R. Maartens, N. Randriamiarinarivo, and A. Baloyi, J. Cosmol. Astropart. Phys. 09 (2019) 025.
[9] S. Sarkar, B. Pandey, and R. Khatri, Mon. Not. R. Astron. Soc. **483**, 2453 (2019).
[10] P. Ntelis, A. J. Hawken, S. Escoffier, A. Ealet, and A. Tilquin, arXiv:1904.06135.
[11] U. Andrade, C. A. P. Bengaly, J. S. Alcaniz, and S. Capozziello, Mon. Not. R. Astron. Soc. **490**, 4481 (2019).
[12] E. Payne, S. Banagiri, P. D. Lasky, and E. Thrane, Phys. Rev. D **102**, 102004 (2020).
[13] B. Pandey and S. Sarkar, J. Cosmol. Astropart. Phys. 07 (2021) 019.
[14] R. S. Gonçalves, G. C. Carvalho, U. Andrade, C. A. P. Bengaly, J. C. Carvalho, and J. Alcaniz, J. Cosmol. Astropart. Phys. 03 (2021) 029.
[15] R.-G. Cai, Y.-Z. Ma, B. Tang, and Z.-L. Tuo, Phys. Rev. D **87**, 123522 (2013).
[16] Z. Chang, H.-N. Lin, Y. Sang, and S. Wang, Mon. Not. R. Astron. Soc. **478**, 3633 (2018).
[17] H.-K. Deng and H. Wei, Eur. Phys. J. C **78**, 755 (2018).
[18] Z. Q. Sun and F. Y. Wang, Mon. Not. R. Astron. Soc. **478**, 5153 (2018).
[19] U. Andrade, C. A. P. Bengaly, B. Santos, and J. S. Alcaniz, Astrophys. J. **865**, 119 (2018).
[20] D. Zhao, Y. Zhou, and Z. Chang, Mon. Not. R. Astron. Soc. **486**, 5679 (2019).
[21] J. P. Hu, Y. Y. Wang, and F. Y. Wang, Astron. Astrophys. **643**, A93 (2020).
[22] W. Rahman, R. Trotta, S. S. Boruah, M. J. Hudson, and D. A. van Dyk, Mon. Not. R. Astron. Soc. **514**, 139 (2022).
[23] D. J. Schwarz and B. Weinhorst, Astron. Astrophys. **474**, 717 (2007).
[24] A. Kashlinsky, F. Atrio-Barandela, D. Kocevski, and H. Ebeling, Astrophys. J. Lett. **686**, L49 (2008).
[25] I. Antoniou and L. Perivolaropoulos, J. Cosmol. Astropart. Phys. 12 (2010) 012.
[26] B. Kalus, D. J. Schwarz, M. Seikel, and A. Wiegand, Astron. Astrophys. **553**, A56 (2013).
[27] M. Yoon, D. Huterer, C. Gibelyou, A. Kovács, and I. Szapudi, Mon. Not. R. Astron. Soc. **445**, L60 (2014).
[28] P. Tiwari and A. Nusser, J. Cosmol. Astropart. Phys. 03 (2016) 062.
[29] B. Javanmardi, C. Porciani, P. Kroupa, and J. Pflamm-Altenburg, Astrophys. J. **810**, 47 (2015).
[30] J. Colin, R. Mohayaee, M. Rameez, and S. Sarkar, Mon. Not. R. Astron. Soc. **471**, 1045 (2017).
[31] K. Migkas, G. Schellenberger, T. H. Reiprich, F. Pacaud, M. E. Ramos-Ceja, and L. Lovisari, Astron. Astrophys. **636**, A15 (2020).
[32] K. Migkas, F. Pacaud, G. Schellenberger, J. Erler, N. T. Nguyen-Dang, T. H. Reiprich, M. E. Ramos-Ceja, and L. Lovisari, Astron. Astrophys. **649**, A151 (2021).
[33] N. J. Secrest, S. von Hausegger, M. Rameez, R. Mohayaee, S. Sarkar, and J. Colin, Astrophys. J. Lett. **908**, L51 (2021).
[34] T. M. Siewert, M. Schmidt-Rubart, and D. J. Schwarz, Astron. Astrophys. **653**, A9 (2021).
[35] O. Luongo, M. Muccino, E. O. Colgáin, M. M. Sheikh-Jabbari, and L. Yin, Phys. Rev. D **105**, 103510 (2022).
[36] C. Krishnan, R. Mohayaee, E. O. Colgáin, M. M. Sheikh-Jabbari, and L. Yin, Phys. Rev. D **105**, 063514 (2022).
[37] M. G. Dainotti, B. De Simone, T. Schiavone, G. Montani, E. Rinaldi, and G. Lambiase, Astrophys. J. **912**, 150 (2021).
[38] Y. Hoffman, D. Pomarede, R. Brent Tully, and H. Courtois, Nat. Astron. **1**, 0036 (2017).
[39] E. J. Shaya, R. B. Tully, D. Pomarède, and A. Peel, Astrophys. J. **927**, 168 (2022).
[40] J. Koda, C. Blake, T. Davis, C. Magoulas, C. M. Springob, M. Scrimgeour, A. Johnson, G. B. Poole, and L. Staveley-Smith, Mon. Not. R. Astron. Soc. **445**, 4267 (2014).
[41] Y.-Z. Ma, C. Gordon, and H. A. Feldman, Phys. Rev. D **83**, 103002 (2011).
[42] W. A. Hellwing, A. Nusser, M. Feix, and M. Bilicki, Mon. Not. R. Astron. Soc. **467**, 2787 (2017).
[43] D. Huterer, D. Shafer, D. Scolnic, and F. Schmidt, J. Cosmol. Astropart. Phys. 05 (2017) 015.
[44] C. A. P. Bengaly, J. Larena, and R. Maartens, J. Cosmol. Astropart. Phys. 03 (2019) 001.
[45] M. A. Strauss and J. A. Willick, Phys. Rep. **261**, 271 (1995).
[46] H. J. Macpherson and A. Heinesen, Phys. Rev. D **104**, 023525 (2021).

[47] S. Dhawan, A. Borderies, H. J. Macpherson, and A. Heinesen, arXiv:2205.12692.
[48] J. Kristian and R. K. Sachs, Astrophys. J. **143**, 379 (1966).
[49] G. F. R. Ellis, S. D. Nel, R. Maartens, W. R. Stoeger, and A. P. Whitman, Phys. Rep. **124**, 315 (1985).
[50] P. B. Lilje, A. Yahil, and B. J. T. Jones, Astrophys. J. **307**, 91 (1986).
[51] H. M. Courtois, Y. Hoffman, R. B. Tully, and S. Gottlöber, Astrophys. J. **744**, 43 (2012).
[52] S. L. Parnovsky and A. S. Parnowski, Astrophys. Space Sci. **343**, 747 (2013).
[53] N. Aghanim *et al.* (Planck Collaboration), Astron. Astrophys. **641**, A1 (2020).
[54] K. M. Górski, E. Hivon, A. J. Banday, B. D. Wandelt, F. K. Hansen, M. Reinecke, and M. Bartelman, Astrophys. J. **622**, 759 (2005).
[55] D. M. Scolnic, D. O. Jones, A. Rest, Y. C. Pan, R. Chornock, R. J. Foley, M. E. Huber, R. Kessler, G. Narayan, A. G. Riess *et al.*, Astrophys. J. **859**, 101 (2018).
[56] J. Guy, M. Sullivan, A. Conley, N. Regnault, P. Astier, C. Balland, S. Basa, R. G. Carlberg, D. Fouchez, D. Hardin *et al.*, Astron. Astrophys. **523**, A7 (2010).
[57] M. Smith, R. C. Nichol, B. Dilday, J. Marriner, R. Kessler, B. Bassett, D. Cinabro, J. Frieman, P. Garnavich, S. W. Jha *et al.*, Astrophys. J. **755**, 61 (2012).
[58] M. Sako *et al.* (SDSS Collaboration), Publ. Astron. Soc. Pac. **130**, 064002 (2018).
[59] A. G. Riess, R. P. Kirshner, B. P. Schmidt, S. Jha, P. Challis, P. M. Garnavich, A. A. Esin, C. Carpenter, R. Grashius, R. E. Schild *et al.*, Astron. J. **117**, 707 (1999).
[60] S. Jha, R. P. Kirshner, P. Challis, P. M. Garnavich, T. Matheson, A. M. Soderberg, G. J. M. Graves, M. Hicken, J. F. Alves, H. G. Arce *et al.*, Astron. J. **131**, 527 (2006).
[61] M. Hicken, W. M. Wood-Vasey, S. Blondin, P. Challis, S. Jha, P. L. Kelly, A. Rest, and R. P. Kirshner, Astrophys. J. **700**, 1097 (2009).
[62] M. Hicken, P. Challis, S. Jha, R. P. Kirshner, T. Matheson, M. Modjaz, A. Rest, W. M. Wood-Vasey, G. Bakos, E. J. Barton *et al.*, Astrophys. J. **700**, 331 (2009).
[63] M. Hicken, P. Challis, R. P. Kirshner, A. Rest, C. E. Cramer, W. M. Wood-Vasey, G. Bakos, P. Berlind, W. R. Brown, N. Caldwell *et al.*, Astrophys. J. Suppl. Ser. **200**, 12 (2012).
[64] C. Contreras, M. Hamuy, M. M. Phillips, G. Folatelli, N. B. Suntzeff, S. E. Persson, M. Stritzinger, L. Boldt, S. González, W. Krzeminski *et al.*, Astron. J. **139**, 519 (2010).
[65] S. A. Rodney, A. G. Riess, L.-G. Strolger, T. Dahlen, O. Graur, S. Casertano, M. E. Dickinson, H. C. Ferguson, P. Garnavich, B. Hayden *et al.*, Astron. J. **148**, 13 (2014).
[66] O. Graur, S. A. Rodney, D. Maoz, A. G. Riess, S. W. Jha, M. Postman, T. Dahlen, T. W. S. Holoien, C. McCully, B. Patel *et al.*, Astrophys. J. **783**, 28 (2014).
[67] A. G. Riess, S. A. Rodney, D. M. Scolnic, D. L. Shafer, L.-G. Strolger, H. C. Ferguson, M. Postman, O. Graur, D. Maoz, S. W. Jha *et al.*, Astrophys. J. **853**, 126 (2018).
[68] A. G. Riess, L.-G. Strolger, S. Casertano, H. C. Ferguson, B. Mobasher, B. Gold, P. J. Challis, A. V. Filippenko, S. Jha, W. Li *et al.*, Astrophys. J. **659**, 98 (2007).
[69] N. Suzuki, D. Rubin, C. Lidman, G. Aldering, R. Amanullah, K. Barbary, L. F. Barrientos, J. Botyanszki, M. Brodwin, N. Connolly *et al.*, Astrophys. J. **746**, 85 (2012).
[70] R. B. Tully, H. M. Courtois, and J. G. Sorce, Astron. J. **152**, 50 (2016).
[71] R. B. Tully, H. Courtois, Y. Hoffman, and D. Pomarède, Nature (London) **513**, 71 (2014).
[72] D. J. Fixsen, E. S. Cheng, J. M. Gales, J. C. Mather, R. A. Shafer, and E. L. Wright, Astrophys. J. **473**, 576 (1996).
[73] R. B. Tully, E. J. Shaya, I. D. Karachentsev, H. M. Courtois, D. D. Kocevski, L. Rizzi, and A. Peel, Astrophys. J. **676**, 184 (2008).
[74] C. Marinoni, P. Monaco, G. Giuricin, and B. Costantini, Astrophys. J. **505**, 484 (1998).
[75] S. S. Boruah, M. J. Hudson, and G. Lavaux, Mon. Not. R. Astron. Soc. **498**, 2703 (2020).
[76] T. Hong, C. M. Springob, L. Staveley-Smith, M. I. Scrimgeour, K. L. Masters, L. M. Macri, B. S. Koribalski, D. H. Jones, and T. H. Jarrett, Mon. Not. R. Astron. Soc. **445**, 402 (2014).
[77] S. J. Turnbull, M. J. Hudson, H. A. Feldman, M. Hicken, R. P. Kirshner, and R. Watkins, Mon. Not. R. Astron. Soc. **420**, 447 (2012).
[78] A. Nusser and M. Davis, Astrophys. J. **736**, 93 (2011).
[79] M. I. Scrimgeour, T. M. Davis, C. Blake, L. Staveley-Smith, C. Magoulas, C. M. Springob, F. Beutler, M. Colless, A. Johnson, D. H. Jones *et al.*, Mon. Not. R. Astron. Soc. **455**, 386 (2016).
[80] J. Carrick, S. J. Turnbull, G. Lavaux, and M. J. Hudson, Mon. Not. R. Astron. Soc. **450**, 317 (2015).
[81] S. Appleby, A. Shafieloo, and A. Johnson, Astrophys. J. **801**, 76 (2015).
[82] C. L. Steinhardt, A. Sneppen, and B. Sen, Astrophys. J. **902**, 14 (2020).
[83] P. K. Aluri *et al.*, arXiv:2207.05765.
[84] D. Zhao, Y. Zhou, and Z. Chang, Mon. Not. R. Astron. Soc. **486**, 5679 (2019).
[85] D. D. Kocevski and H. Ebeling, Astrophys. J. **645**, 1043 (2006).
[86] E. Kourkchi, R. B. Tully, S. Eftekharzadeh, J. Llop, H. M. Courtois, D. Guinet, A. Dupuy, J. D. Neill, M. Seibert, M. Andrews *et al.*, Astrophys. J. **902**, 145 (2020).
[87] A. G. Riess *et al.*, Astrophys. J. Lett. **934**, L7 (2022).
[88] C. Clarkson and R. Maartens, Classical Quantum Gravity **27**, 124008 (2010).
[89] H. J. Macpherson, arXiv:2209.06775.